Best
Available
Copy

AD-A010 913

ACOUSTICALLY SCANNED IMAGE

Gordon S. Kino

Stanford University

Prepared for:

Office of Naval Research
Advanced Research Projects Agency

February 1975

DISTRIBUTED BY:

NTIS

National Technical Information Service
U. S. DEPARTMENT OF COMMERCE

174090

ADA010913

Microwave Laboratory
W. W. Hansen Laboratories of Physics
Stanford University
Stanford, California

ACOUSTICALLY SCANNED IMAGE

Semiannual Report No. 1

1 August 1974 – 31 January 1975

Contract: N00014-67-A-0112-0084

ARPA Order No. 2778

Program Code No. 4D10

Scientific Officer:

Director, Physics Program
Physical Sciences Division
Office of Naval Research
Department of the Navy
800 North Quincy Street
Arlington, Virginia 22217

M. L. Report No. 2410

February 1975

Gordon S. Kino
Principal Investigator
(415) 497-0205

Sponsored by

Advanced Research Projects Agency

ARPA Order No 2778

TABLE OF CONTENTS

ACOUSTICALLY SCANNED IMAGE

I. SUMMARY

We describe here our work during the last six months on a new type of optical scanning device which makes use of acoustic surface waves to scan an optical image. The device employs a silicon semiconductor as the photodetector; the nonlinear interaction of two acoustic surface waves, whose electric fields interact with the silicon is employed in the basic mechanism of detection. In this mode of operation, this nonlinear mechanism basically measures the variation of the capacity of the depletion layer of the semiconductor rather than the conduction current through the depletion layer, as is normally the case in most solid-state devices. The readout mechanism is essentially a nondestructive one, and the definition of the device is controlled basically by the bandwidth of the acoustic surface wave signal employed, while the number of resolvable spots is equal to the time-bandwidth product of the surface wave device. The measured sensitivities of some of these devices are of the order of 1 $\mu W/cm^2$ although, because of the presence of surface states, our results have varied quite widely at the present time from one device to another.

In Section II we describe our work on the airgap Si-$LiNbO_3$ convolver configuration which is employed in this optical imaging device. It has proved convenient to work with this configuration because of our experience with earlier convolvers based on this type of construction and because it is simple to change the semiconductor samples that are employed so as to test out the principles of operation. We do not regard this configuration as a final one;

we regard it more as a laboratory tool for testing out our research ideas when they are first conceived. Thus in Section II we describe our work on scanning optical images with the airgap convolver, and how we are able to obtain directly, in this device, Fresnel and Fourier spatial transforms of an optical image. We also describe how we have reconstructed the original images by carrying out inverse transforms. In the case of the Fresnel transforms, we do this by inserting the output signal, which is in the form of an rf chirp, into a dispersive delay line. In the case of the Fourier transform, we take the inverse transform by using a spectrum analyzer.

The employment of such transforms gives a major improvement in signal-to-noise ratio because of the large scanning times employed for one spot. We show theoretically that by this technique one can improve the signal-to-noise ration by a factor NB_{in}/B_{out} where N is the number of spots, B_{in} is the bandwidth of the scanning signals employed in the device, and B_{out} is the bandwidth after processing. This ratio B_{in}/B_{out} is also equal to the ratio of the final scan time in the display to the scan time in this device. Improvements in the signal-to-noise ratio of the order of 30 dB are easily realizable in practice, as we will show. Further advantages of this technique are that we are able to obtain an arbitrarily narrow output bandwidth and an arbitrary scan rate. Pictures with a 20 μsec line time and a 30 point resolution have been obtained in this way, and we are currently on the point of testing a system with 100-300 resolvable spots. This part of the work will be completed when a new dispersive delay line filter, which is being supplied to us by Lincoln Laboratories, becomes available.

In Section III we describe our theoretical development of the semiconductor convolver theory. This is required for an understanding of the operation of the optical imaging device, so as to be able to determine the optimum operating conditions. We were particularly interested in understanding the effect of surface states, i.e., whether it would be useful to operate with a depletion layer at the surface, at flat band conditions or in accumulation. We have shown that a depleted surface is the optimum condition in which to operate, both for optical imaging and for convolution devices. The results we have obtained theoretically are in good agreement with our experiments and yield an entirely new way of measuring the surface state density distribution through the bandgap.

A complete theory for the optical sensitivity of these devices is not as yet fully developed, basically because in our design of the ZnO on Si convolver, described in Section IV, somewhat different configuration and considerations are used and should result in several orders of magnitude improvement in optical sensitivity. Therefore, it has not seemed worthwhile to carry out the complete theory for the present configuration, although we feel that our work for the past six months has led us to a basic physical understanding of how the sensitivity depends on the operating parameters of the devices.

In Section IV we describe our development of the technology of the ZnO on Si convolver configuration for use in the optical imaging device. It has been our contention all along that the airgap - $LiNbO_3$ - Si convolver configuration is only a step on the way to the development of a practical imaging device. It is not the final configuration, because 1) the airgap is mechanically difficult to work with, and 2) it is more difficult to obtain a device

which is free of surface state problems in the SiO_2 on the Si interface when the SiO_2 is exposed to the atmosphere rather than being covered by a layer of metal or other material. It appears that the outside surface of the SiO_2 tends to retain surface charges; other effects, which we do not fully understand, also appear to be present and tend to lead to nonuniformities in such devices.

The development of a ZnO on Si convolver has required a considerable improvement in the technology. This we have been carrying out, partly in the Stanford Integrated Circuit Laboratory and partly in our Acoustic Laboratory, using both technologies where needed. The requirement has been, first, to obtain high quality ZnO which is consistent from run-to-run and in which the piezoelectric coupling is at its optimum value. This we have succeeded in doing very satisfactorily, after considerable development. Secondly, we have required high quality transducers for use in this configuration; this has required considerable development. One problem has been that, because the transducers are laid down very close to the silicon surface, the capacity of the pads is very high and we have had to construct special transducers to minimize this capacity. Also we have had to operate in a balanced mode with specially constructed balun transformers used to improve the efficiency. We are now able to reproducibly make devices with a net terminal loss from terminal-to-terminal of less than 15 dB, using transducers with a bandwidth of 8 MHz and a center frequency of 125 MHz. We expect to improve the bandwidth by a factor of 2 or 3. This should make the device adequate for a 500 spot image with a semiconductor length of 2 cm. It should be pointed out that

most of the development time during this part of the development of the technology has been involved with improving the convolver itself, rather than using the ZnO-Si configuration for optical imaging. We have now made convolvers whose operating characteristics are comparable to those of the airgap convolver. We have also worked with waveguide configuration on another contract and, by narrowing the beam down, have been able to make a highly efficient convolver. We have shown that the present configuration is optically sensitive, although we have also found that there are storage effects present which are dependent on surface states. Thus, considerable effort has also been devoted to minimizing these storage effects. For this purpose, we are presently constructing a buried channel device which should eliminate most of these difficulties.

Finally, in Section V we give a short description of a chirp generator, which we have constructed on this contract, for use in transform coding in these types of devices. The need here is to be able to make chirp generators with a high scan rate and a highly linear frequency variation with time.

For use on this contract, we have purchased an optical bench which includes a set of lenses and a light source. In addition, two waveform generators for use in the transform devices have been purchased. We have also constructed an FM chirp generator in this laboratory which has better linearity for the scan rates and bandwidths we require than commercially available generators. This is described in Section V of this report.

II. IMAGING AND TRANSFORM CODING

A. Introduction

We describe here new techniques for scanning optical images. These techniques make use of the signal processing methods familiar in the acoustic surface wave device field. In particular, it has proved advantageous to use linearly modulated FM chirps for scanning, rather than simple pulses. This has the effect of giving an arbitrary scan time, and makes it possible to carry out Fourier transforms of optical images; in other cases, it is possible to obtain chirp Fresnel transforms of optical images. The advantage of using such methods is that the signal-to-noise ratio can be considerably enhanced, and the bandwidth of the image signal can be tailored and unnecessary information eliminated from the image.

B. Basic Configuration of the Convolver and Theory

We consider the silicon-acoustic surface wave-delay line configuration illustrated in Fig. II-1. A semiconductor, such as silicon, is placed in close proximity to the surface of the delay line, typically made of $LiNbO_3$. When the device is operated as a simple convolver, two waves are launched at the same frequency ω in opposite directions by means of interdigital transducers. These waves have fields that vary as $\exp[j\omega(t+x/v)]$ and $\exp[j\omega(t-x/v)]$ respectively, where v is the surface wave velocity. In the simplest regime, the "depletion" regime, the total electric field E normal to the surface produces a depletion layer of thickness l where $E = qN_d l/\epsilon$;

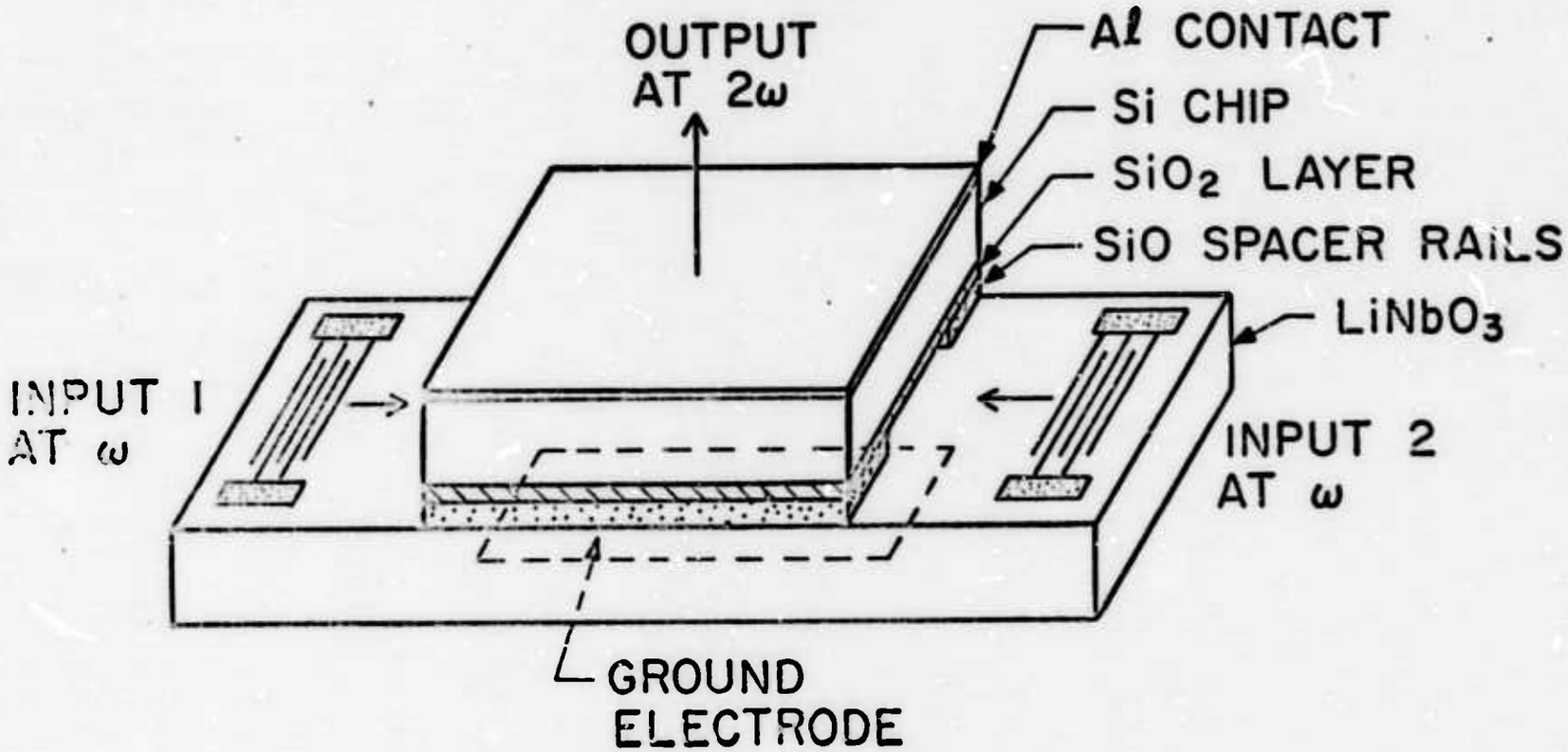

FIG. II-1 -- Schematic of the semiconductor convolver.

N_d is the donor density of the assumed n-type semiconductor, q the electronic charge, and ϵ the permittivity of the semiconductor. In turn, this implies that there will be a potential developed across the depletion layer $\phi = qN_d l^2/2\epsilon$, or

$$\phi = \epsilon E^2/2qN_d \quad . \qquad \text{(II-1)}$$

Because of this nonlinearity, a uniform potential will be generated at a frequency 2ω . It can be detected between the silicon and a plane electrode on the lower surface of the delay line. This resultant potential represents the convolution of the input signal modulations.

In order to lower the surface state density, the semiconductor surface is carefully oxidized. This is particularly important when biasing the semiconductor or when illuminating it, so as to change the carrier density of the silicon and hence the output of the convolver, enabling construction of a photo-sensitive device.

C. Application of the Convolver to Imaging

Since the silicon used is photoconductive, illuminating it modulates the carrier density and hence the nonlinear coupling. The simplest way to read-out an image is to insert a narrow rf pulse, the scanning pulse, at one end, and a long pulse at the other end of the delay line. The convolution output will be modulated and the output as a function of time corresponds to the illumination along one line of the image. One of the original difficulties of this system was its limited dynamic range because of the inherently high output with

no light present (the dark current). A big advance in the state of the art has been to make the dark current very small and hence the dynamic range large. We do this by passing the light incident on the semiconductor through a coarse optical grating of period l, as shown in Fig. II-2. This, in effect, introduces a wavenumber K into the light beam, such that $Kl = 2\pi$.

Now the optimum output is obtained with two input signals of frequencies ω_1, ω_2, propagation constants of k_1, k_2 respectively such that

$$k_1 - k_2 = \pm K , \tag{II-2a}$$

$$\omega_1 - \omega_2 = \pm Kv , \tag{II-2b}$$

where v is the velocity of the acoustic surface wave. By using a nondegenerate system with input frequencies ω_1, ω_2 displaced by the amount given in Eq. (II-2b) a strong output is obtained when the device is illuminated, with a very small output when there is no light. Thus the "dark current" is caused to be very small. It should be noted that if three colored gratings of different periodicities are used, the device can be arranged to give outputs at three different frequencies corresponding to the three primary colors.

With the simple set-up represented in Fig. II-3 and a displacement in frequency of 10 MHz, we have obtained a dynamic range of the order of 30 dB. An example of "direct imaging" with a narrow scanning pulse and a grating of periodicity 350 μm (10 MHz) is shown in Fig. II-4. We are now developing a system accommodating a 20 MHz frequency displacement. A dynamic range of 35 dB or more has been obtained. The dynamic range is now limited only by the noise level in the device, i.e., its sensitivity.

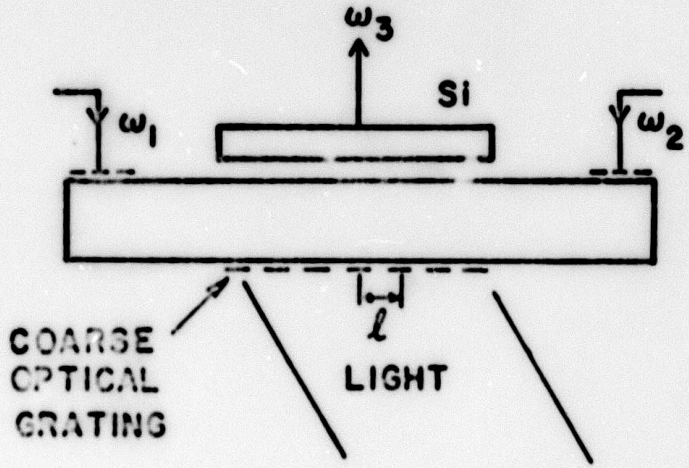

$$k\ell = 2\pi$$

$$k_1 - k_2 \pm k = 0$$

$$\omega_1 - \omega_2 = \pm kv$$

$$\omega_3 = \omega_1 + \omega_2$$

FIG. II-2 -- Schematic of imager with low dark current.

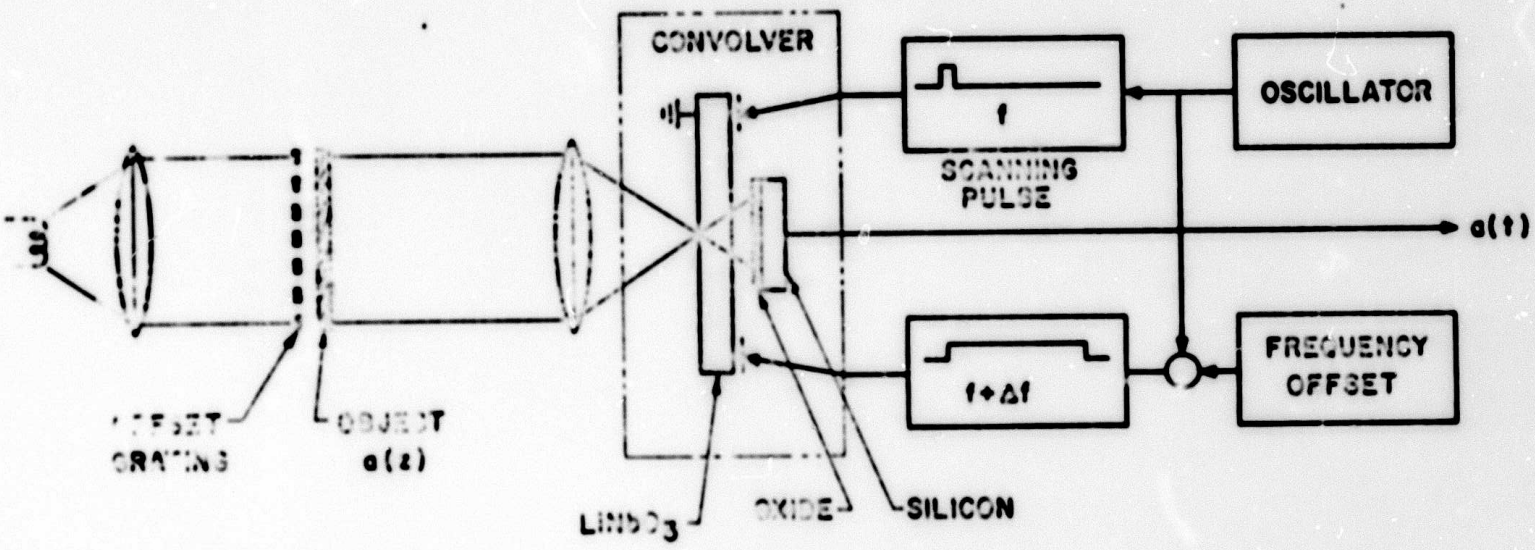

(a)

FIG II-3 -- Schematic of the system used for direct imaging.

Best Available

Copy

for all Pictures

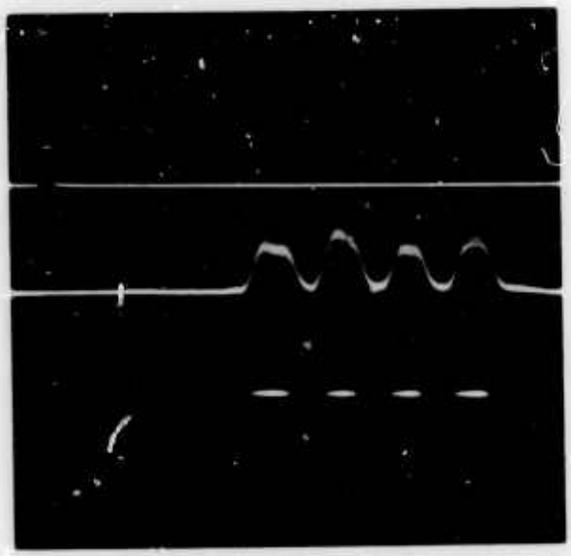

SCANNING PULSE .15 μ sec

A-SCAN

B-SCAN

.5 μ sec

FIG. II-1--Direct imaging of a [illegible] ns period pattern. Input frequencies [illegible], and 115 MHz.

The convolution output voltage is proportional to $1/N$. When the convolver is illuminated, the carrier density is perturbed by ΔN ; and due to the grating, this perturbation is of the form $\Delta N = \Delta N_0 + \Delta N_1 \cos Kz$. If the input signal center frequencies are identical, the convolver is operated in a degenerate mode and its output voltage is proportional to $(N + \Delta N_0)^{-1}$ or

$$V_{deg} \propto \frac{1}{N}\left(1 - \frac{\Delta N_0}{N}\right) . \qquad \text{(II-3)}$$

If the input signal center frequencies are offset by $\Delta\omega = \pm Kv$, the convolver is operated in a nondegenerate fashion; it only responds to one of the harmonic components of ΔN , hence its output voltage is proportional to ΔN_1 , or

$$V_{nondeg} \propto \frac{1}{N} \cdot \frac{1}{2} \frac{\Delta N_1}{N} . \qquad \text{(II-4)}$$

The ratio $\Delta N/\Delta N_0$ is simply a function of the geometry of the grating; in the experimental case of a grating composed of dark stripes three times wider than the white stripes (duty cycle = 0.25) we obtain

$$\Delta N_1/N_0 = 4\sqrt{2}/\pi . \qquad \text{(II-5)}$$

To check the validity of the relations (II-3) and (II-4), we measured the decrease in the degenerate convolution power corresponding to a certain illumination. From this measurement and Eq. (II-3) we derive $\Delta N_0/N$; then using Eqs. (II-4) and (II-5) we can predict the value of

$$\left(\frac{1}{2} \frac{\Delta N_1}{N}\right)^2$$

i.e., the ratio of the nondegenerate convolution power to the degenerate convolution power in absence of light. This ratio was measured directly for a small offset of 0.4 MHz so that diffusion effects may be neglected. The results are compared in the table given below and show a good agreement between predictions and measurements.

$\frac{P_{deg} \text{ with light}}{P_{deg} \text{ no light}}$ (measured)	P_{nondeg}/P_{deg} no light	
	predicted	measured
- 3 dB	- 11.7 dB	-12.5 ± .5 dB

In the flat band case, a simple equilibrium model predicts a variation of the surface carrier concentration given by the relation

$$\Delta N_1 = \Delta P_1 \sim G/\alpha D \cdot [(L^{-2} + K^2)^{+1/2} + S/D]^{-1} \quad , \qquad \text{(II-6)}$$

where G is the generation rate, α the light attenuation in the silicon, D, L, and S the diffusion coefficient, the diffusion length and the surface recombination velocity of the minority carriers, respectively.

In the case of n-type silicon with a surface state concentration not exceeding $10^{11} cm^{-2}$ it will be seen that the term S/D can be neglected.

Figure II-5 gives plots of the ratio of the nondegenerate convolution power to the degenerate one in absence of light, versus the frequency offset for two n-type silicon samples. This ratio should be proportional to ΔN_1^2. As can be seen from Fig. II-5 the dependence on K predicted by Eq. (II-6) is

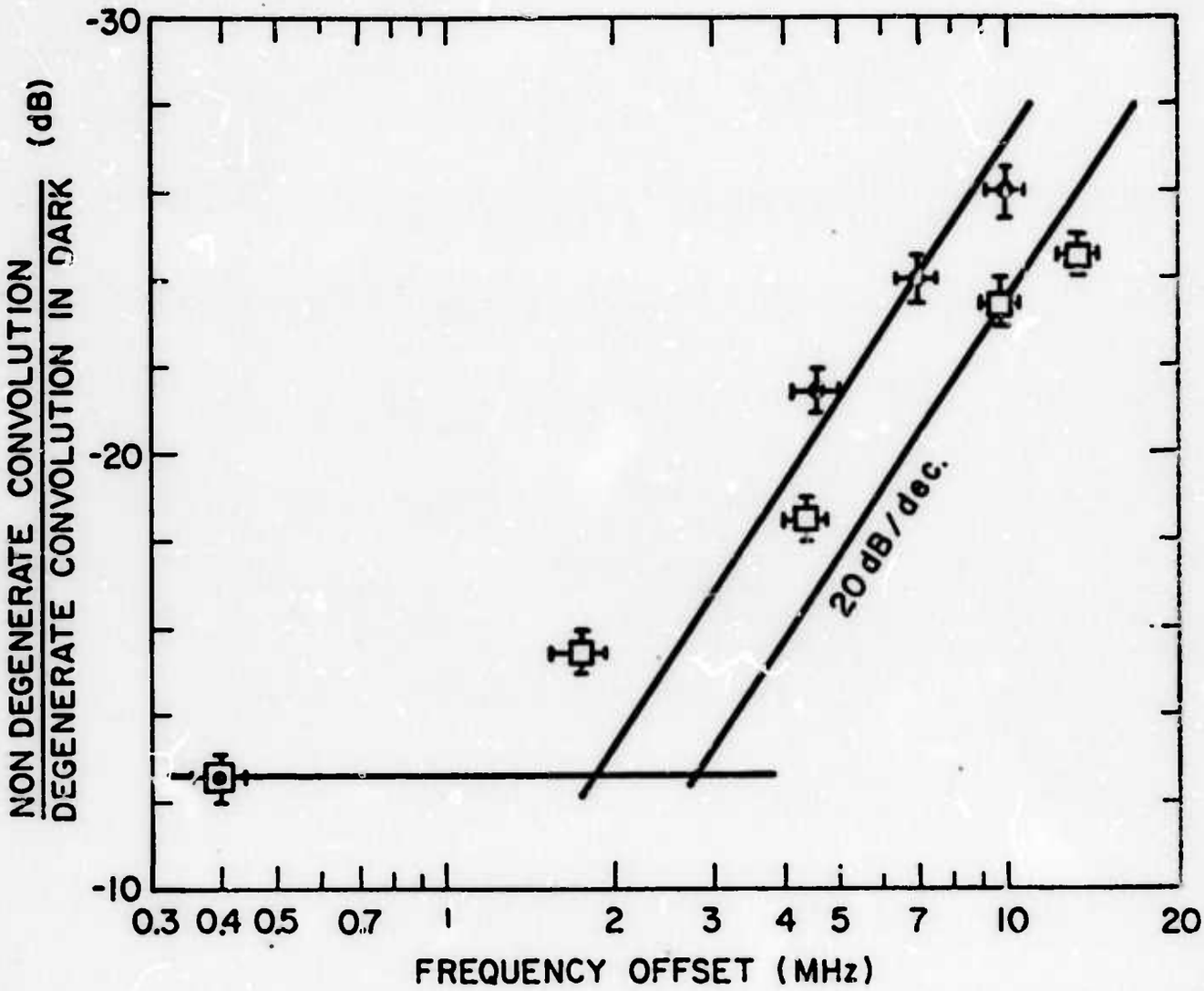

FIG. II-5--Ratio of nondegenerate convolution power to degenerate convolution power in dark versus frequency offset for two n-type silicon samples, under flat band conditions.

verified experimentally: for small K the nondegenerate convolution is independent of K ; for large K it varies as K^{-2} ; the break-off point takes place for a frequency offset of 2.5 ± 0.5 MHz, i.e., $K = 5 \pm 1.10^3 m^{-1}$. From Eq. (II-6) this point corresponds to $K = L^{-1}$, hence we can measure the value of the minority carrier lifetime $\tau = L^2/D$. We obtain $\tau = 60 \pm 20$ μs. The light sensitivity depends on the nature of the semiconductor and the value of the surface potential. The threshold sensitivity has been measured to vary from 1 to 100 $\mu W/cm^2$. The MTF of the system depends on whether the surface is at flat band or is depleted and has not been fully evaluated for the depleted case. Suffice it to say that an advantage of the use of the periodic grating is that the MTF is almost independent of the definition. We expect and observe far better sensitivity with a depleted surface, due to the high hole velocity normal to the surface.

D. Transform Techniques

So far we have discussed the simplest situation — that of a short pulse scan of the image. This is equivalent to scanning a semiconductor with an electron beam of small diameter. In such a device the signal-to-noise ratio decreases as the time taken to scan one spot in the image is decreased, i.e., as the definition is increased. We now consider the possibility of using more complicated waveforms of long-time duration (the line time) to scan one line of the image. In this case, if we feed the output into a correctly designed matched filter, as in radar systems, it is possible to obtain a short pulse signal corresponding to a spot in the image, i.e., to take an inverse transform of the scanning signal. As in radar, such matched filter pulse compression techniques give rise to an improvement in the signal-to-noise ratio because any spot in the image is now scanned for the line time rather than the spot time.

As an example, when two linear FM chirp signals are inserted into opposite ends of the device with frequencies $\omega_a = \omega_1 + \mu_1 t$, $\omega_b = \omega_2 - \mu_2 t$, respectively; they give rise to two waves with a linear variation of frequency and a square law variation of phase. Using the center of the device as a reference, we find that phase of the resultant product signal is

$$\phi(z,t) = \phi_a + \phi_b = (\omega_1 + \omega_2)t + (\omega_2 - \omega_1)\frac{z}{v} + \frac{\mu_1}{2}\left(t - \frac{z}{v}\right)^2 - \frac{\mu_2}{2}\left(t + \frac{z}{v}\right)^2 \quad . \quad \text{(II-7)}$$

With a grating filter with $K = (\omega_2 - \omega_1)/v$, the output signal due to a carrier density variation $n(z)$ along the length of the devices, caused by illumination with light is

$$F(t) = e^{j(\omega_1+\omega_2)t} \int n(z)\, e^{j\frac{\mu_1-\mu_2}{2}\left(t^2 + \frac{z^2}{v^2}\right)} \times e^{-j(\mu_1+\mu_2)\frac{tz}{v}}\, dz \quad . \qquad \text{(II-8)}$$

When $\mu_1 = \mu_2 = \mu$, the output as a function of time is the spatial Fourier transform of the carrier density, and hence of one line of the image. By using an acoustic convolver, or matched chirp filter, and inserting this signal in the proper way, an inverse Fourier transform of the input signal can be obtained, and hence the original image signal recovered.

The device offers the important advantages that (1) it tends to differentiate against impulse noise because impulse noise modulation of the Fourier transform signal gives rise to a uniform background on the image rather than points of light, (2) the Fourier transform or other transforms can be employed for signal processing to enhance the signal-to-noise ratio, to eliminate redundant information in the pictures, and to obtain an arbitrary scan rate

along the imaging device, (3) because the input frequencies are different, we can feed in signals of arbitrary length without reasons to worry about echoes off the end of the line and multiple transit convolutions.

We have carried out several experiments to demonstrate these principles which are illustrated in Fig. II-6. In one example, a grating filter with a 350 μm period is used in front of the device to give good dynamic range. An object consisting of a photographic transparency is also placed in the path of the incident light, and a signal corresponding to the Fourier transform of the object is produced, as shown in Fig. II-7(a). In this case the input signals were 10 msec long chirps of opposite sign with center frequencies of 115 and 105 MHz. In the examples shown, we used a simple 7 period grating with a periodic spacing of approximately 2 mm as the illuminated object, and displayed the output amplitude as a function of time, as shown in Fig. II-7(a). The center peak corresponds to the zero spatial frequency component and the two main lobes to the periodicity of the grating.

With a slow scan such as the one used here, the simplest way to reconstitute the image is with a spectrum analyzer. The output from the spectrum analyzer is shown in Fig. II-7(b), and is seen to correspond well to the configuration of the original object.

It is apparent that the output bandwidth is determined by the chirp rate, and that the Fourier transform technique samples, any point on the image for the whole length of the chirp. Thus the use of this technique provides a considerable enhancement of the signal-to-noise ratio, as compared to employing a direct narrow pulse scan.

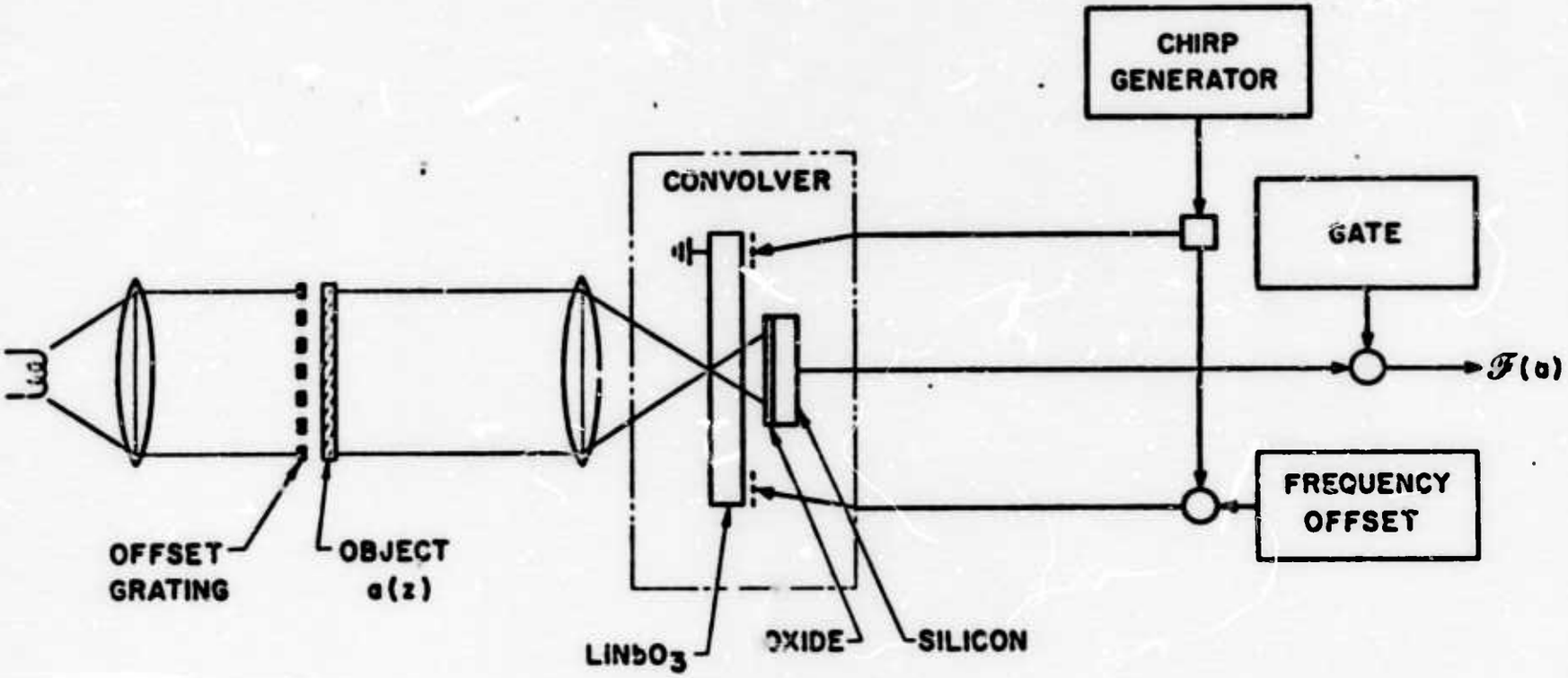

FIG. II-6 -- Schematic of the system used for taking a Fourier transform.

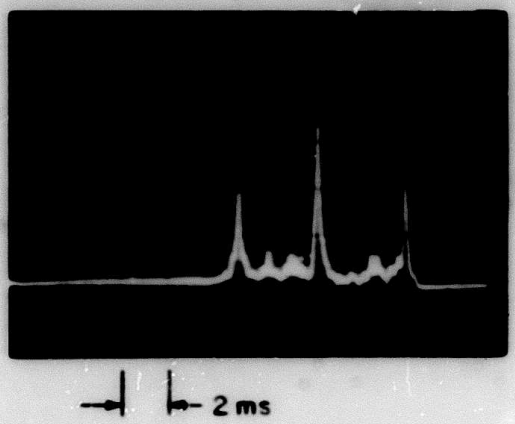

(a)

FOURIER TRANSFORM

FIG. II-7(a) -- A Fourier transform of a periodic grating with a period of 2 ms. A grating filter of 350 μm spacing was used with input frequencies of 115 and 105 MHz and chirps with a total excursion of 2.5 MHz and 10 ms.

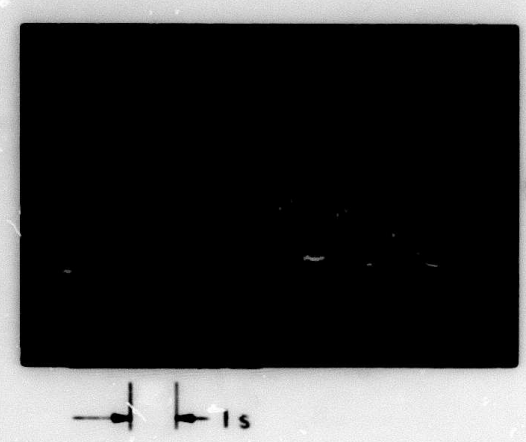

(b)

INVERSE TRANSFORM

= IMAGE

FIG. II-7(b) -- The inverse Fourier transform taken with a spectrum analyzer.

The Fourier transform technique is merely one example of a wide range of signal processing techniques which can be applied for optical image processing, not only to improve the sensitivity but also the bandwidth and definition.

In the more general case, with $\mu_1 \neq \mu_2$, a Fresnel transform is obtained. We have demonstrated such a Fresnel transform system as shown in Fig. II-8. In this case, a chirp output with a chirp rate $\mu_1 - \mu_2$ and a bandwidth $B_s = (\mu_1 - \mu_2)\, T_C/2\pi$ is obtained from one spot at z_0 in the image $[n(z) = \delta(z_0)$ in the integral of Eq. (II-8)]. The image can be reconstructed by inserting the output signal into a suitably matched filter, matched to a chirp with a rate $\mu_1 - \mu_2$.

In the Appendix, a rigorous mathematical derivation of the entire process is given. It is shown how the chirped signals have to be chosen to achieve a given resolution. One conclusion is that if we suppose that the time length of the chirps is T_C, the minimum resolvable spot, defined as the distance between 4 dB points equivalent to the Rayleigh criterion is of length d_s where

$$d_s = 2\pi v/(\mu_1 + \mu_2)T_C = v/B_C \quad . \qquad \text{(II-9)}$$

Thus B_C is the total bandwidth of the chirps, or the bandwidth required for the pulse scan of the minimum resolvable spot. In this case it can be shown that the effective scan velocity along the convolver becomes

$$v_s = v(\mu_1 - \mu_2)/(\mu_1 + \mu_2) \quad . \qquad \text{(II-10)}$$

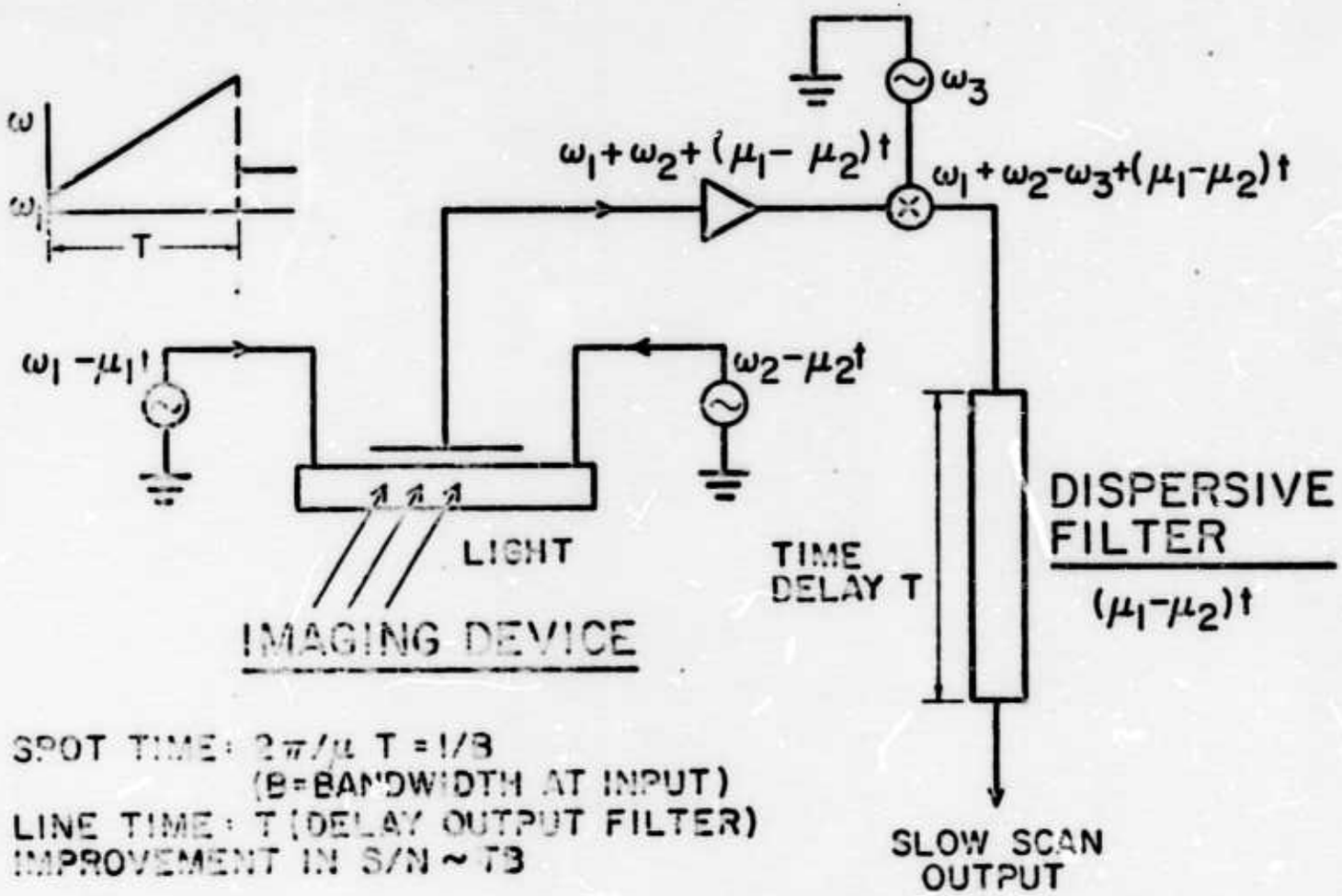

FIG. II-6 -- A schematic of the complete imaging system using Fresnel transforms.

Thus an arbitrary scan velocity can be obtained. The number of resolvable spots is still $N = L/d_s$, where L is the length of the imaging device.

It is also shown in the appendix that the optimum signal-to-noise ratio improvement in using this matched filter chirped scan is

$$G = N(B_C/B_s) = N(v/v_s) = T_C v/d_s \quad . \qquad \text{(II-11)}$$

There is an improvement of B_C/B_s because the bandwidth of the noise entering the matched filter is decreased by that factor; and there is a factor N , the number of resolvable spots which arises because of the large increase in the time spent obtaining a signal from one particular spot in the image.

For a TV line, $T_C = 60\ \mu s$, $B_s = 5$ MHz , $N = 300$, we would use an acoustic device with a delay of $T_A = 6\ \mu s$ and a chirp bandwidth $B_C = 50$ MHz ; the signal-to-noise ratio improvement would be 60×50 , i.e. 35 dB . The initial experiments were done with the suboptimal figures $T_C = 20\ \mu s$, $B_s \sim 1.5$ MHz , $B_C = 7.5$ MHz leading to a 30 point resolution. Examples of pictures taken with this device, by mechanically scanning in one direction are shown in Fig. II-9.

FIG. II-9 -- Pictures taken with the system shown in Fig. II-8. The chirp excursions are 4.5 and 5.0 MHz for 20 μs, the resolution is approx. 50 points, the number of lines is approx. 20.

III. THE AIRGAP CONVOLVER

A. Complete Theory

A simple theory valid for flat band condition has been published in this laboratory.[1] A new and more complete theory covering the depletion, accumulation, and inversion regimes will now be described. This will be compared with experimental results in Section B. It is shown that we can predict the shape of the variation of the propagation loss with applied dc voltage, and can accurately predict the convolution efficiency with variation of the applied dc voltage. The use of this theory allows us to obtain a direct measure of the surface state densities in silicon. It also provides a good understanding of the physical processes underlying the convolution phenomenon. These results are new and far more complete than the previous theory available. They lead to an entirely new technique for measurement of the surface state density distribution through the bandgap, as well as being of fundamental importance to our understanding of the operation of the convolver and imaging device.

1. General Discussion

In this study, we shall compute the open circuit convolution output voltage, denoted by V_{op} and we shall refer it to the acoustic powers; this means that we do not take into account the transducer and output circuit loss. We shall write V_{op} as

$$V_{op} = \alpha V_0 \quad ,$$

V_0 is the open circuit output voltage computed assuming no propagation loss

under the semiconductor, $L = 20 \ln_{10}\alpha$, is the propagation loss due to the presence of the semiconductor. If a normal surface displacement field D_s is created at the surface of the semiconductor, we shall see that a potential ϕ_s is generated across the device, which has the following form

$$\phi_s = AD_s + BD_s^2 \quad .$$

We now assume two oppositely traveling waves are present with fields $D_s^{(1)}$ and $D_s^{(2)}$ at the surface of the semiconductor, with acoustic potentials $\phi_a^{(1)}$ and $\phi_a^{(2)}$ and powers $P_a^{(1)}$ and $P_a^{(2)}$. The "nonlinear convolution" voltage generated is

$$V_0 = BD_s^{(1)}D_s^{(2)} \quad .$$

It can be rewritten as

$$V_0 = B\left(\frac{D_s^{(1)}D_s^{(2)}}{\phi_a^{(1)}\phi_a^{(2)}}\right) \cdot \left(\frac{\phi_a^{(1)}\phi_a^{(2)}}{\sqrt{P_a^{(1)}P_a^{(2)}}}\right) \cdot \sqrt{P_a^{(1)}P_a^{(2)}}$$

where B is the nonlinear coupling coefficient; it will be derived in Section A.2 by integration of Poisson's equation. The expression

$$\frac{D_s^{(1)}D_s^{(2)}}{\phi_a^{(1)}\phi_a^{(2)}} = \left(\frac{D_s^{(1)}}{\phi_a^{(1)}}\right)^2$$

is the linear gap coupling; it will be derived in Section A.3 by use of

an equivalent circuit concept. The expression below

$$\frac{\phi_a^{(1)}\phi_a^{(2)}}{\sqrt{P_a^{(1)}P_a^{(2)}}} = 2Z_a$$

is twice the acoustic impedance of the piezoelectric used. This will be reviewed in Section A.4.

The loss term L is also a linear term and hence will be obtained in Section A.3.

2. <u>The Nonlinear Coupling</u>

We may determine the potential at the surface of the semiconductor by writing Poisson's equation in the form

$$\frac{d^2\phi}{dy^2} = \frac{qN_d}{\epsilon}\left[\exp\left(\frac{q\phi}{kT}\right) - 1\right] - \frac{qn_i^2}{\epsilon N_d}\left[\exp\left(-\frac{q\phi}{kT}\right) - 1\right] \quad , \qquad \text{(III-1)}$$

where the symbols have their usual meanings. Integrating once by multiplying by $d\phi/dy$ and writing $D = -\epsilon d\phi/dy$, we find that at the surface of the semiconductor denoted by the subscript s

$$D_s^2 = N_d kT\epsilon\, F^2(q\phi_s/kT) \qquad \text{(III-2)}$$

where the function F is defined[2] as

$$F(v) = \sqrt{2}\left(\exp v - v - 1 + \frac{n_i^2}{N_d}\left[\exp(-v) + v - 1\right]\right)^{1/2} \quad . \qquad \text{(III-3)}$$

If a DC bias V_G is applied to the semiconductor, we write potential and

displacement as

$$\phi_s = \phi_{s0} + \phi_{s1}$$

$$D_s = D_{s0} + D_{s1} \quad ,$$

where the subscripts 0 and 1 refer to DC and RF terms, respectively. We solve Eq. (III-2) for ϕ_s to second order in D_s by writing

$$\phi_s = AD_s + BD_s^2 \quad . \tag{III-4}$$

It follows that

$$A = 2D_{s0}\left[a(\exp u_0 - 1) - b\left(\exp(-u_0) - 1\right)\right]^{-1} \tag{III-5}$$

$$B = \left[a(\exp u_0 - 1) - b\left(\exp(-u_0) - 1\right)\right]^{-1} \times \left\{1 - \frac{\frac{2q}{kT}\left(a \exp u_0 + b \exp(-u_0)\right)}{a\left(\exp(u_0) - 1\right) - b\left(\exp(-u_0) - 1\right)} D_{s0}^2\right\} , \tag{III-6}$$

where

$$u_0 = q\phi_{s0}/kT \ ; \ a = 2qN_d\epsilon \ ; \ b = 2qn_i^2\epsilon/N_d$$

$$D_{s0} = \sqrt{N_d kT\epsilon} \cdot F(q\phi_{s0}/kT) \cdot \mathrm{sgn}(\phi_{s0}) \quad . \tag{III-7}$$

For an n-type semiconductor and flat band condition, where $D_{s0} = 0$, $A = \lambda_d/\epsilon$ and $B = 1/2qN_d\epsilon$. When the surface is well depleted $A = d/\epsilon$, $B = 1/2qN_d\epsilon$ where d is the length of the depletion layer and λ_d the Debye length. When the surface is strongly accumulated or inverted $A \to 0$, $B \to 0$. A complete plot of $BqN_d\epsilon$ vs $q\phi_{s0}/kT$ is given in Fig. III-1 for

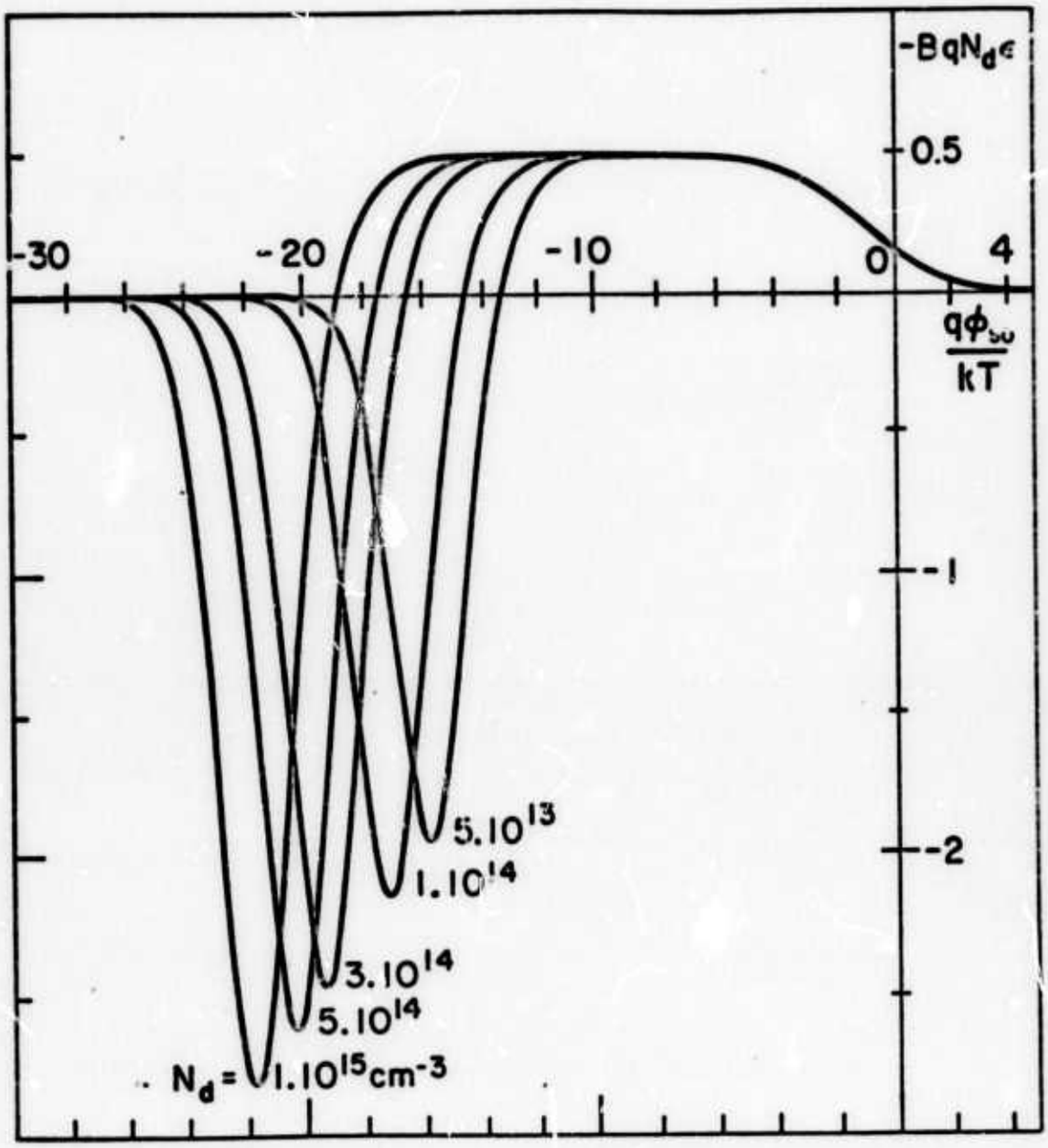

FIG. III-1 -- Plot of the nonlinear coupling coefficient B vs the DC surface potential.

various concentrations N_d . B changes sign and goes through a maximum when the surface is nearly intrinsic. In that regime, ϕ_{s0} is a very rapidly varying function of V_G . Besides the carrier concentration is very low and the minority carriers, in particular, cannot follow the rapidly varying traveling wave field in order to stay in thermal equilibrium. For all purposes the semiconductor behaves as if it were only depleted. For stronger inversion ($BqN_d\epsilon < 0.5$) the minority carrier concentration becomes large, their time constant becomes shorter and they can now follow the acoustic field, by drifting rapidly from regions of low field to regions of high field. To summarize, the curves of Fig. III-1 will not be used near their zeros and maxima.

Equation (III-7) allows us to relate the bias voltage V_G to the DC surface potential ϕ_{s0} . Because of the high capacitance of the piezoelectric (thickness y_p = 1 to 3 mm , permittivity $\epsilon_{yy} \sim 70$) compared to the airgap capacitance (0.1 to 0.5 μm, $\epsilon_0 = 1$), all the voltage is dropped across the piezoelectric. If D_{s0} is the DC displacement in the piezoelectric we can write

$$V_G = D_{s0}\, y_p/\epsilon_{yy} \qquad \text{(III-8)}$$

and from Eq. (III-7), ϕ_{s0} is given by

$$V_G = \frac{y_p}{\epsilon_{yy}} \sqrt{N_d kT\epsilon} \cdot F(q\phi_{s0}/kT) \cdot \mathrm{sgn}(\phi_{s0}) \quad . \qquad \text{(III-9)}$$

3. <u>Equivalent Circuit</u>

To relate the first order term in ϕ_s to the value of D_s , we use an equivalent electrical circuit in which "current" is displacement current

$I = j\omega D$ and "potential" is electric potential ϕ . The admittance is then

$$Y = j\omega D/\phi \quad .$$

To derive this circuit we shall make extensive use of the Kino-Reeder perturbation theory[3] for the Rayleigh wave amplifier.

<u>Flat Band Conditions</u>. Following Kino-Reeder, the admittance Y^- at the surface of the semiconductor looking at the piezoelectric through the airgap is given by Eq. (21) of reference 3:

$$\frac{1}{Y^- - Y_0} = j\left[\frac{M(\beta h)}{\beta w Y_0} - \frac{\beta w Z_a(\beta h)}{\beta'^2 - \beta^2}\right] \qquad \text{(III-10)}$$

where

$$Y_0 = j\beta w \epsilon$$

$$M(\beta h) = \frac{\epsilon_0 + \epsilon_p \tanh(\beta h)}{(\epsilon_0 + \epsilon_p)\left(1 + \tanh(\beta h)\right)} \quad .$$

β' is the perturbed propagation constant, β the unperturbed one; h is the airgap height, w the width of the acoustic beam, $Z_a(\beta h)$ the acoustic impedance at the surface of the semiconductor and $\epsilon_p = (\epsilon_{yy}\epsilon_{zz} - \epsilon_{yz}^2)^{1/2}$ is the equivalent permittivity of the piezoelectric. Similarly the admittance Y^- looking into the semiconductor assumed semi-infinite is given by Eq. (45) of reference 3:

$$Y^- - Y_s = -\frac{\omega_c \beta \epsilon}{-1 + j(\omega_c/\omega_D)^{1/2}} \quad . \qquad \text{(III-11)}$$

$\omega_c = \mu q N_d/\epsilon$ is the dielectric relaxation frequency for majority carriers; $\omega_D = v^2/(kT/q)\mu$ is the diffusion frequency; μ is the majority carrier mobility. From Eqs. (III-10) and (III-11) we can draw an equivalent circuit shown in Fig. III-2 where we ignore Y_{inv}, C_{dep}. The piezoelectric is modeled by the inductance $\mathcal{L}_a$ across the driving source ϕ_a. The gap coupling is represented by the capacitance C_{gap} and the bulk of the semiconductor contains a lossy term R_b and a capacitive term C_b. The respective expressions are given below:

$$\mathcal{L}_a = \frac{1}{\omega}\frac{\beta w Z_a(\beta h)}{\beta'^2 - \beta^2}$$

$$C_{gap} = \beta\epsilon_0/M(\beta h) \qquad \text{(III-12)}$$

$$R_b = (\omega_c \epsilon\beta)^{-1}$$

$$C_b = (\omega_c \omega_D)^{1/2}\,\beta\epsilon/\omega = \epsilon/\lambda_d \quad .$$

It will be noted that for the semiconductors of interest the loss term is small

$$R_b \ll 1/(C_b\omega) \quad .$$

The "linear gap coupling" term D_s/ϕ_a is now straightforward to evaluate

$$D_s/\phi_a = \frac{\beta\epsilon_0}{M(\beta h)}\left(1 + \frac{\beta\epsilon_0\,\lambda_d}{\epsilon M(\beta h)}\right)^{-1} \quad . \qquad \text{(III-13)}$$

The term $\beta\epsilon_0\lambda_d/\epsilon M(\beta h)$ in Eq. (III-13) is a correction term of the order of 10% or less for 10 to 100 Ω-cm silicon.

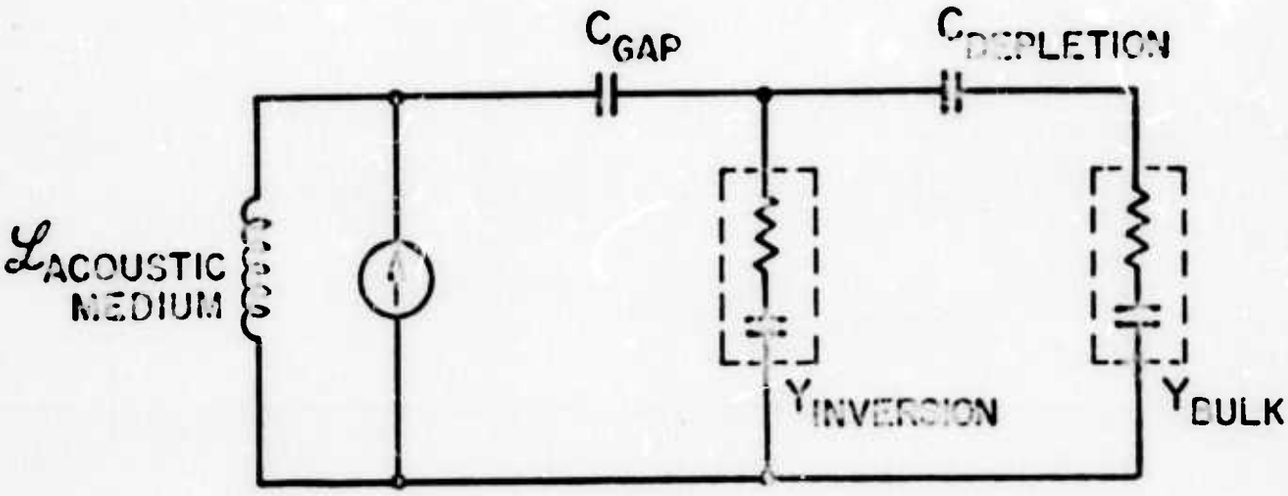

FIG. III-2 -- Equivalent circuit used in the evaluation of linear coupling and loss.

Accumulation Conditions. Extra majority carriers are now accumulated at the surface of the semiconductor. The excess charge distribution near the surface and its center of mass L_c can be computed (see reference 2). Thus we can derive an equivalent uniform surface concentration N_{accu}

$$N_{accu} = N_d + \Delta N/2L_c \quad , \qquad \text{(III-14)}$$

where ΔN is the total excess charge. The gap coupling is still given by Eq. (III-13) where λ_d is now computed for a concentration N_{accu}. Only the correction term is affected and it becomes even smaller.

Depletion Conditions. We use the simple depletion layer approximation. This introduces an extra capacitance $C_{depletion}$ in series with C_{gap} where

$$C_{depletion} = \epsilon/l \quad . \qquad \text{(III-15)}$$

$l = (2\epsilon\phi_{s0}/qN_d)^{1/2}$ is the depletion length. In other words, the airgap h has now increased to $h + l\epsilon_0/\epsilon$ and all previous results are directly applicable.

Inversion. The depletion width increases until ϕ_{s0} becomes of the order of twice the bulk potential ϕ_B. For larger ϕ_{s0} the depletion width will level off and any increase of surface potential will correspond to an inversion of the surface. The inversion layer extends into the semiconductor. To keep the calculations simple but nevertheless account for the charge spreading, we model the inversion layer as an infinitesimally thin charge sheet located at the true center of mass, a distance L_{ci} away from the surface. This decreases the effective depletion length by L_{ci} and increases the airgap by $L_{ci}\epsilon_0/\epsilon$. The total inversion charge

per unit area is given by

$$\Delta N_i = N_d \lambda_d g^+ \quad . \tag{III-16}$$

And as in the case of accumulation, g^+ and L_{ci} are functions of ϕ_{s0} and they have been plotted by Many, et al.[2] From Eq. (30) of reference 3, the admittance of such a sheet is

$$Y_{inv} = \frac{\omega_{ci} \epsilon \beta^2 \delta}{1 - j\omega/\omega_{Di}} \quad , \tag{III-17}$$

where ω_{ci} and ω_{Di} are the dielectric relaxation and diffusion frequencies, respectively, for minority carriers. δ is the width of the equivalent charge sheet. From Eqs. (III-16) and (III-17), we obtain the admittance of the inversion layer

$$Y_{inv} = \frac{\mu_i q N_d \lambda_d \beta^2 g^+}{1 - j\omega/\omega_{Di}} \tag{III-18}$$

and we can now draw the full equivalent circuit. It is shown in Fig. III-2. To first order, Y_{bulk} is mainly capacitive and Y_{inv} mainly resistive introducing some loss and hence reducing the total current I_T flowing into the semiconductor, therefore reducing the convolution output. This reduction occurs mainly in the inversion regime; it is therefore of interest to evaluate the ratio of I_T in the presence of an inversion (characterized by g^+) to I_T at maximum depletion ($g^+ = 0$):

$$\rho = \left[\frac{I_T(g^+)}{I_T(g^+=0)}\right]^2 = \left[\frac{\phi_a/D_s(g^+)}{\phi_a/D_s(g^+=0)}\right]^2 \quad . \tag{III-19}$$

The "reduction factor" ρ is straightforward to evaluate using the equivalent

circuit, and the plots for L_{ci} and g^+. R is a monotonically decreasing function of g^+ and for $g^+ \sim 10$, which corresponds to a medium inversion, R is of the order of 10^{-1}.

<u>Propagation Loss due to the Semiconductor</u>. The dispersion relation for the semiconductor-airgap-piezoelectric system is obtained by writing that the total impedance in the equivalent circuit is zero. In the expression for $\mathcal{L}_a$ it is convenient to assume that the perturbed acoustic wave has a propagation constant of the form

$$j\beta' = j\beta + \alpha_r + j\beta_r$$

where α_r and β_r are, respectively, the incremental loss and phase delay constants for the system. Equating real and imaginary parts to zero in the dispersion relation yields the propagation loss α_r (in Nepers per meter). In the accumulation and flat band regimes, α_r is found to be inversely proportional to the conductivity. In the depletion regime, the loss decreases due to the increase of the equivalent airgap and in the inversion regime α_r will go through a maximum for $g^+ \sim 10$.

4. <u>Acoustic Impedance</u>

The acoustic potential at the surface of the piezoelectric is related to the acoustic power P_a through the acoustic impedance as follows:

$$\phi_a(0) = \left|2P_a Z_a(0)\right|^{1/2} . \qquad \text{(III-20)}$$

Z_a is given by the perturbation formula Eq. (63) in reference 3:

$$Z_a(0) = \frac{2}{\omega\alpha(\epsilon_p + \epsilon_0)} \left|\frac{\Delta v(0)}{v}\right| . \qquad \text{(III-21)}$$

$|\Delta v(0)/v|$ is the relative surface wave velocity change when a shorting plane is introduced at $y = 0$. Since the rf electric field associated with the surface wave must vary as $\exp(-\beta y)$ in the region $y > 0$, it follows that

$$Z_a(\beta h) = Z_a(0)\exp(-2\beta h) \quad . \qquad \text{(III-22)}$$

B. Theoretical and Experimental Results

1. Flat Band Conditions

We first examine the flat band results. They are of particular use with nonoxidized semiconductor and they provide design curves to select the airgap thickness and the conductivity of the semiconductor.

The convolution efficiency can be normalized, thus defining the $\mathcal{M}$-value as $\mathcal{M} = V_0 w\left(2P_a^{(1)}P_a^{(2)}\right)^{-1/2}$. For flat band conditions, the full expression[1] is

$$\mathcal{M} = \frac{\sqrt{2}\,\epsilon_0}{3qN_d\epsilon(\epsilon_p+\epsilon_0)} \cdot \left|\frac{\Delta v(0)}{v}\right| \frac{\omega}{v^2}\,\frac{\exp(-2\beta h)}{M^2(\beta h)}\left(1+\frac{\beta\epsilon_0\lambda_d}{\epsilon M(\beta h)}\right)^{-2}$$

and the attenuation constant is

$$\alpha_r = \frac{e^2}{qN_d\mu} \cdot \frac{\Delta v}{v^2} \cdot \frac{\epsilon_0^2}{\epsilon(\epsilon_p+\epsilon_0)} \cdot M^{-2}(\beta h) \quad .$$

To obtain this last result we made the assumption that $\omega \ll (\omega_c\omega_D)^{1/2}$, which is justified for most semiconductors of interest. Figures III-3(a) and III-3(b) show plots of the propagation power loss L and plots of $\mathcal{M}$ and $\mathcal{M} \times 10^{-L/2}$ vs conductivity for airgaps varying between 0.1 and 1.0 μm. Both n- and p-type silicons are considered and the operating frequency is 100 MHz.

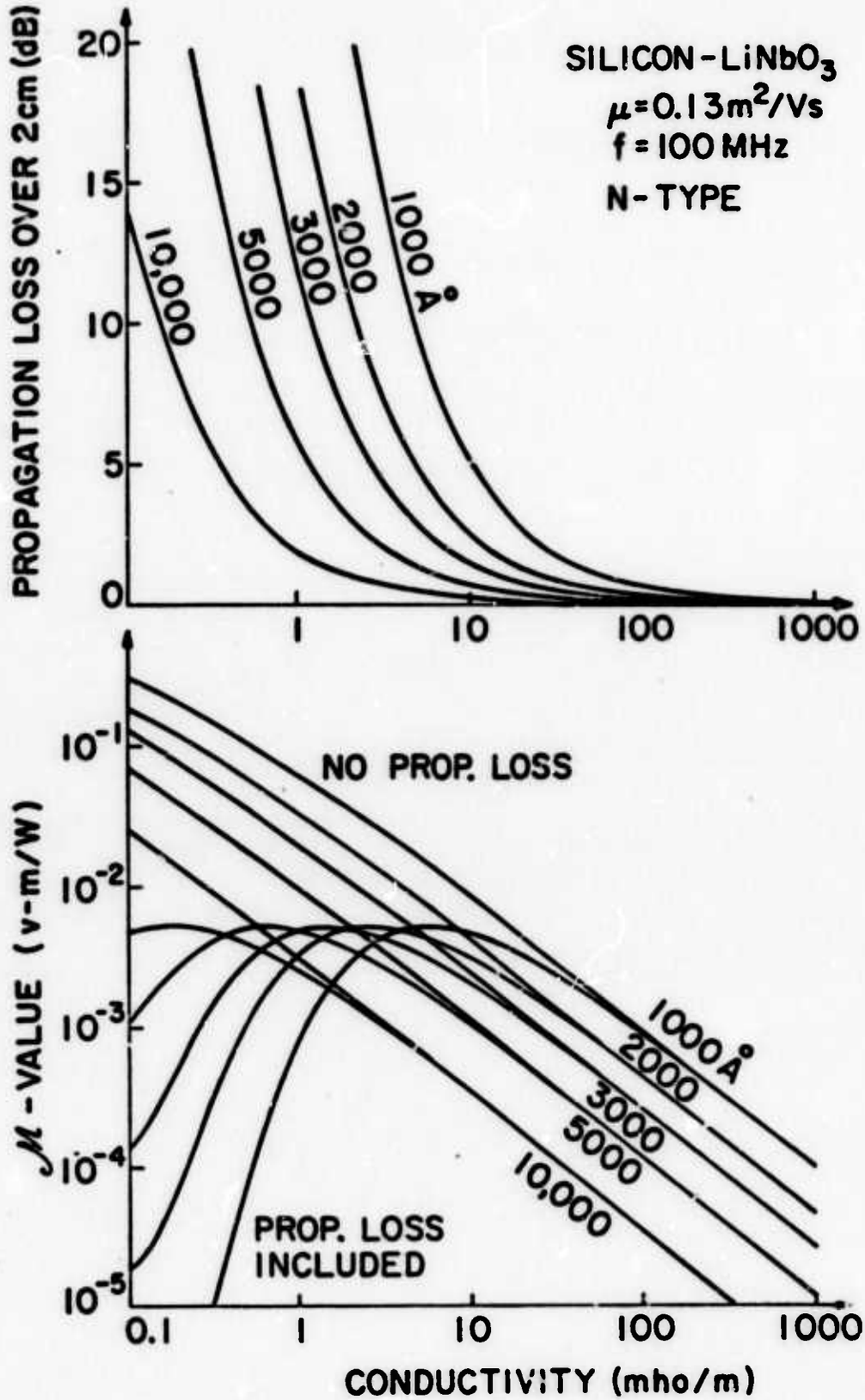

FIG III-3 -- Propagation loss and M-values vs. conductivity for various airgaps.

(a) n-type silicon.

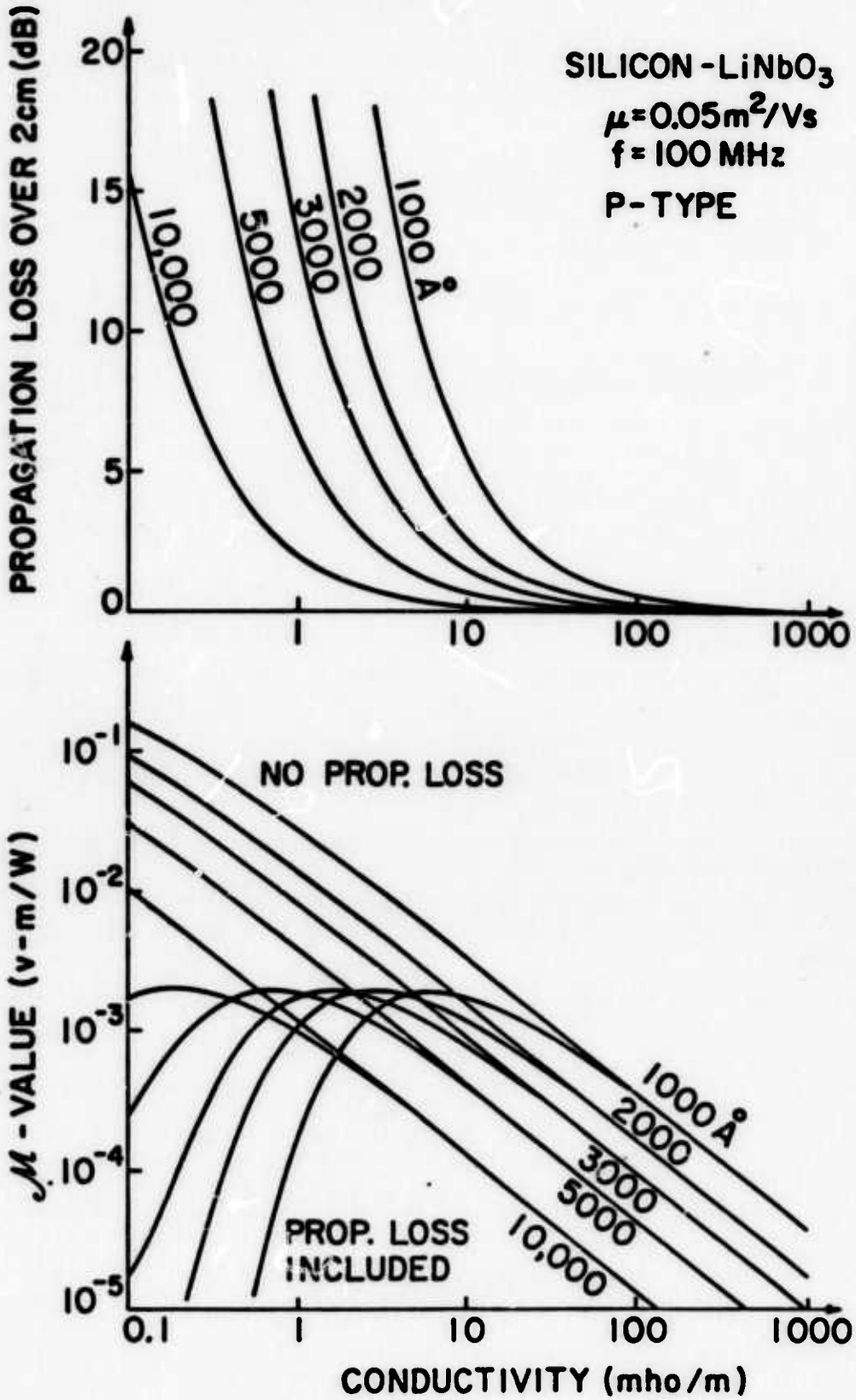

FIG. III-3 -- Propagation loss and μ-values vs conductivity for various airgaps.

(b) p-type silicon.

With non-oxidized silicon, the large surface state density pins down the Fermi level approximately 0.3 V above the valence band edge. For n-type silicon, the deep depletion model of p.30,34 should be used. Some of the experimental results for $\mathcal{M}$ are given in Table I and compared to the theoretical predictions. As can be seen, the agreement is good. (The output circuit was measured and its voltage transfer efficiency computed.)

2. <u>$\mathcal{M}$-Value and Propagation Loss vs Applied Bias Voltage; Off Flat Band Results</u>. In order to be able to control the potential at the surface of the semiconductor, it is necessary to oxidize this surface. This oxidation, when carefully done, will clamp the fast surface state concentration at a low level. By applying a bias voltage to the structure, the energy bands can be bent at the surface relative to the Fermi level. The probability of occupation of the fast surface states will thus vary as a function of the applied bias; so will the charge located in these states (denoted by $Q_{ss} = qN_{ss}$) and the energy distribution. Besides these so-called fast surface states, there also exists at the $Si\text{-}SiO_2$ interface, a fixed charge Q_{fc} independent of the bias. In the case of thermally oxidized silicon, this charge is positive; its magnitude depends on the cleaning and oxidation procedures used. $N_{fc} = Q_{fc}/q$ can be as low as 5.10^9 charges per cm^2. Due to the presence of this positive charge, a p-type silicon surface is depleted or inverted in the absence of any biasing field; an n-type silicon is accumulated. In other words, the theoretical characteristic curves will be shifted towards inversion or accumulation by an amount $V = \frac{Q_{fc}}{C_{oxide}}$. A similar voltage shift will be caused by the fast surface state distribution but, as mentioned previously, this shift will be a function of the bias.

TABLE I

M-Values Theory and Experiment

Semiconductor: n-type Silicon; nonoxidized; 2 cm long

Piezoelectric: YZ $LiNbO_3$; λ = 1.25 mm; h = 1000 - 1500 Å; f = 100 MHz

Si Resistivity (Ω-cm)	7	7	9
2-Port Insertion Loss(1) (dB)	14	22	20
Convolution Efficiency(2) (dB)	-56	-58	-66
Output Circuit Efficiency(3)	0.4	0.7	0.2
M-Value (Experiment)	$5.6\ 10^{-3}$	$6.3\ 10^{-3}$	$7\ 10^{-3}$
M-Value (Theory)(4) (V-m/w)	$6.3\ 10^{-3}$	$6.3\ 10^{-3}$	$7.5\ 10^{-3}$

(1) This includes transducer and propagation losses.

(2) Ratio in dB of output terminal power (in 50 Ω) to product of input terminal powers. All powers in mW.

(3) Ratio of voltage actually developed across a 50 Ω load to open circuit output voltage V_0 .

(4) Computed for h = 1500 Å, assuming deep depletion $\frac{q\phi_{s0}}{kT} = -20$.

We use the results derived in part A to obtain a theoretical plot of the relative $\mathcal{M}$-value vs bias voltage in the accumulation and depletion regimes. As shown in Figs. III-4(a) and III-5(a) we obtain a very good fit with the experimental data if we allow for the presence of a fixed charge at the Si-SiO_2 interface. The p-type semiconductor starts out slightly depleted corresponding to a N_{fc} of 8.10^9 cm^{-2} (90 volt shift). The n-type semiconductor starts out accumulated with a N_{fc} of 9.10^9 cm^{-2} (100 volt shift). Figures III-4(a) and III-5(a) only show relative values of $\mathcal{M}$; absolute values are compared in Table II, now that we know what the flat band voltages are; the agreement is good here too.

As the bias forces the surface of the semiconductor to invert, the Fermi level begins to scan through the fast surface state energy distribution near one edge of the band gap; this will introduce a further shift of the characteristics. In Figs. III-4(a) and III-5(a) the dashed curves are drawn in the absence of any fast states; to account for them these curves must be shifted by an amount ΔV shown in Figs. III-4(b) and III-5(b) as functions of the surface potential $q\phi_{s0}/kT$. The surface state density distribution per unit energy N_{ss} is then obtained by graphical differentiation

$$N_{ss} = \frac{1}{q}\, dQ_{ss}/d\phi_{s0} = \frac{C_{oxide}}{kT}\, d(\Delta V)/d(q\phi_{s0}/kT) \text{ states/cm}^2\text{/eV} \quad .$$

As seen in Figs. III-4(b) and III-5(b), this distribution exhibits maxima near the band edges. Its general shape and amplitude are in accordance with results obtained elsewhere[4] by other methods. The total number of surface states measured in this way is $Q_{ss} = 2.5\ 10^{10}$ cm^{-2} near the conduction band

TABLE II

M-Values Theory and Experiment

Semiconductor: Silicon; 1000 Å SiO_2 layer; 2 cm long

Piezoelectric: YZ-$LiNbO_3$; w = 1.25 mm; f = 100 MHz

Silicon type	N	P
resistivity (Ω-cm)(*)	7	60
Airgap (Å)	1500	3000
2-port insertion loss(1) (No bias) (dB)	16	30
Convolution efficiency(2) (No bias) (dB)	-66	-74
Output circuit efficiency(3)	0.25	0.20
M-value (Experiment, No bias)	$2.8\ 10^{-3}$	$8.8\ 10^{-3}$
M at flat band/M at 0V. Bias(4)	1.7	0.6
M-value at flat band (Expt)	$4.8\ 10^{-3}$	$5.3\ 10^{-3}$
M-value at flat band (Theory) (V-m/W)	$4.5\ 10^{-3}$	$5\ 10^{-3}$

(*) from MOS C-V Measurements

(1), (2), (3) See Table I.

(4) from Fig. III.5(a) and III.6(a).

edge and $Q_{ss} = 5.2 \times 10^{10} cm^{-2}$ near the valence band edge. It is comparably harder to accumulate strongly than to invert a semiconductor, consequently the surface state distribution could only be studied at one extremity of the bandgap with a given semiconductor.

With all this knowledge, we can now plot the theoretical propagation loss due to the semiconductor in all regimes [see Fig. III-4(a) and III-5(a)]. The depletion layer approximation is not very accurate in accounting for the propagation loss. The theoretical loss is also somewhat higher than experimentally observed in inversion. The inversion layer uniformity is indeed a very sensitive function of the uniformity of the airgap and we noticed that only portions of the surface were inverted; the transmission loss was hence lower than expected. Besides, the model we used for the inversion layer is quite simple and may not be very accurate for light inversion when the inversion layer extends several Debye lengths into the bulk. But the general shape and orders of magnitudes can be correctly predicted and in the case of the $\mathcal{M}$-value, the agreement is excellent.

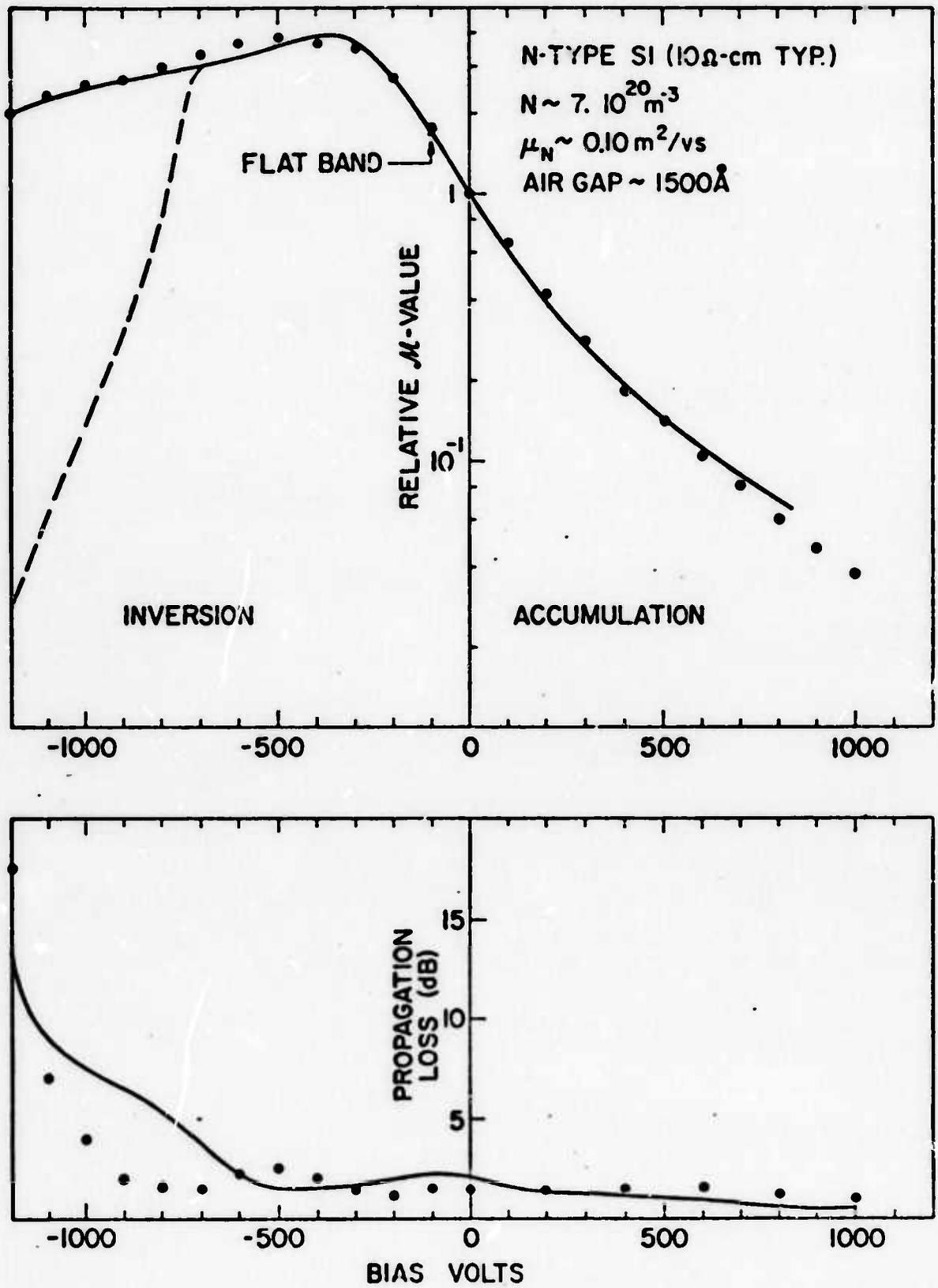

FIG. III-4(a) -- μ-value and propagation loss vs bias voltage (n-type silicon).

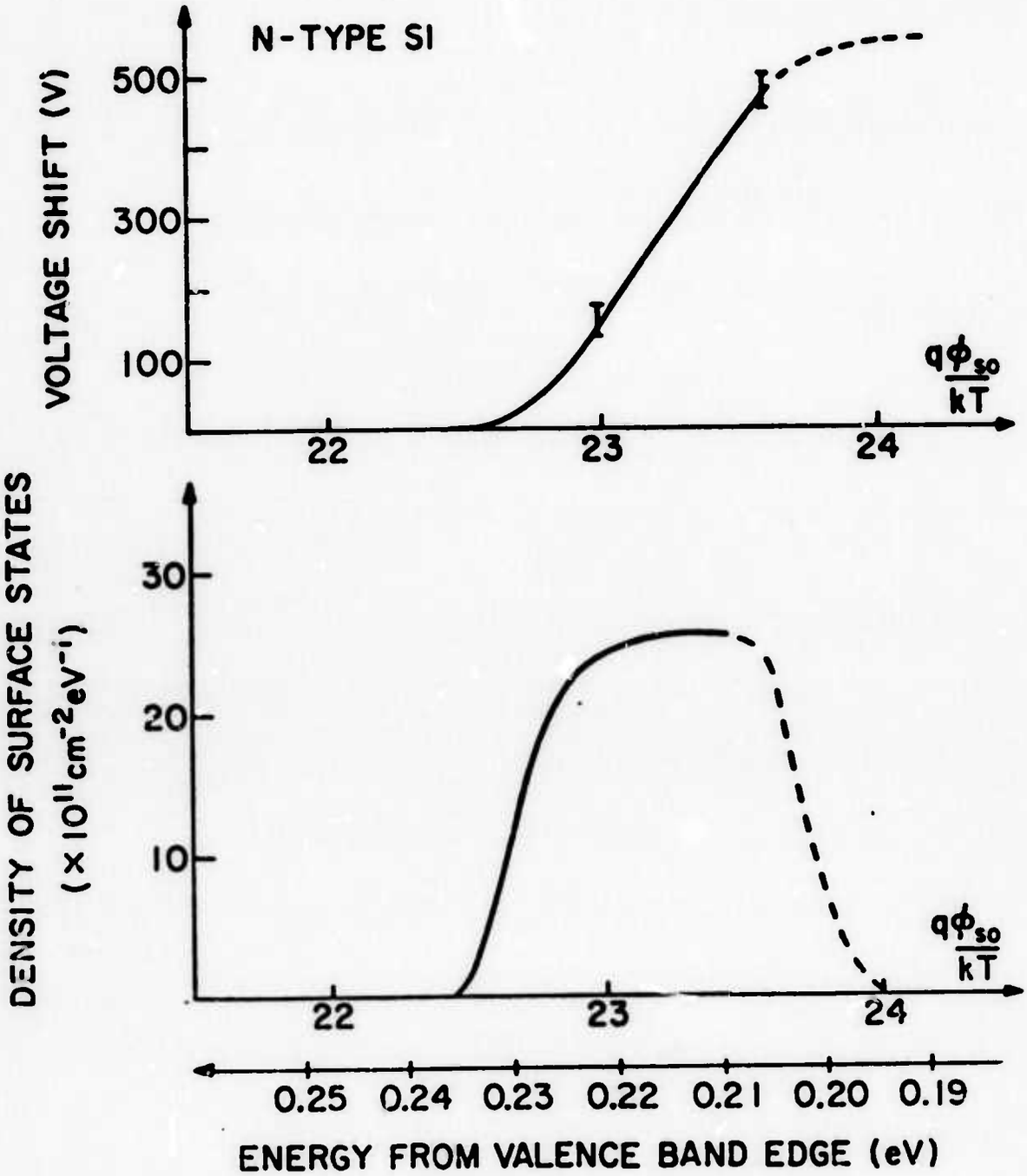

FIG. III-4(b) -- Voltage shift and donor-type surface state density distribution (n-type silicon).

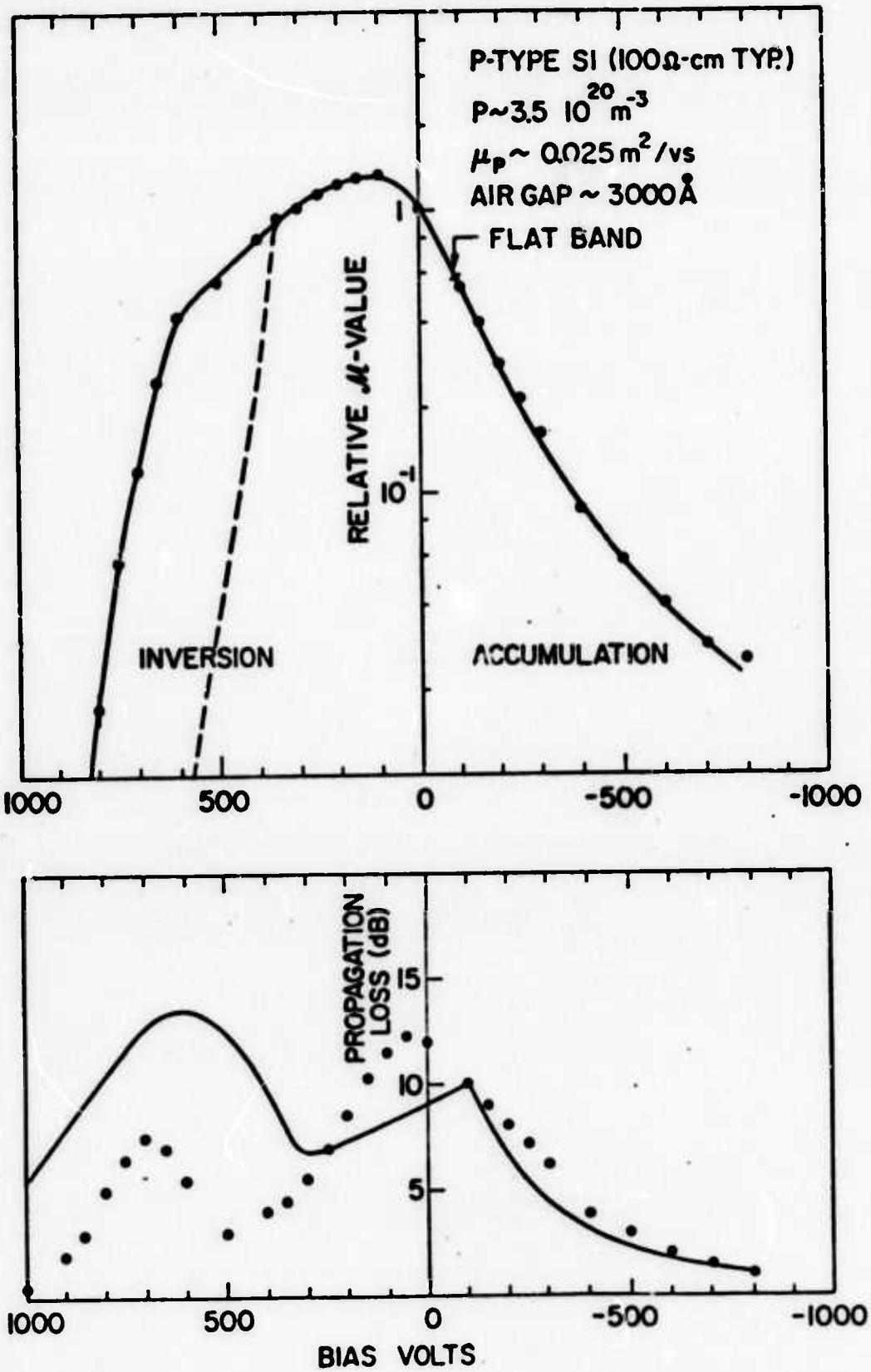

FIG. III-5(a) -- μ-value and propagation loss vs bias voltage (p-type silicon).

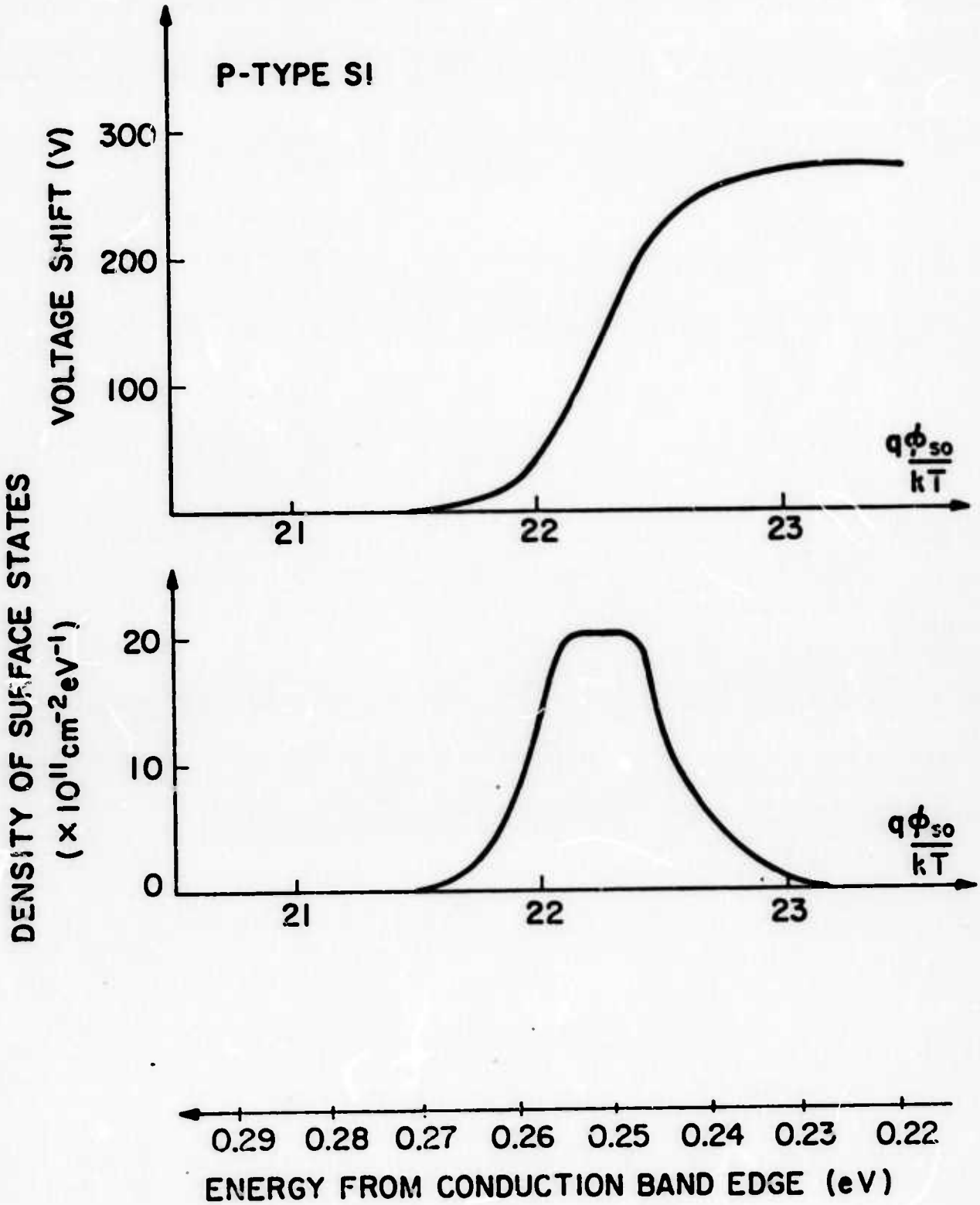

FIG. III-5(b) -- Voltage shift and acceptor-type surface state density distribution (p-type silicon).

IV. MONOLITHIC ZnO ON SILICON CONVOLVER

In Section III we described our work on the airgap convolver for use as an optical imaging device. It is apparent that this configuration, because of its mechanical deficiencies as well as certain problems associated with a free oxide surface, is not likely to be useful in a final device. But, it has been and still is extremely useful for testing out our initial concepts. We have, therefore, devoted considerable effort to the development of a monolithic device. This approach, the deposition of ZnO on Si, has required a considerable technological effort, for it is necessary to perfect the sputtering of the ZnO, to perfect the interdigital transducers required, to understand the theory of the ZnO convolver, and to determine theoretically the optimum thicknesses of the ZnO and the optimum resistivity of Si. We have had to grow special epitaxial layers of Si for this purpose, and learn how to sputter the optimum ZnO, both on the Si and in the regions of the transducers. Beyond this point, we have to concern ourselves with the optical problems, the perfection of a good transparent conducting layer through which the light can reach the Si, problems with traps in the ZnO-SiO_2 interface, and problems with the SiO_2-Si interface in which the surface state density is not necessarily optimum because of the requirements on temperature while growing the ZnO.

We have, therefore, been carrying out a joint effort with B.T. Khuri-Yakub, working on another contract (RADC), to perfect the technology of the ZnO on Si convolver. As time progresses, and we are near to this state at the present time, we intend that the work on this contract will then be devoted exclusively to the optical imaging aspects, while the work on the

RADC contract will be devoted to the development of the convolver for signal processing applications.

The basic configuration employed is shown in Fig. IV-1. It consists of a bulk Si substrate, or an epitaxial layer of n on n^+ Si. Approximately 800 Å of SiO_2 is thermally grown on the Si, then Au pads are laid down on each end of the device. It is vital that the Au crystallites should be well aligned in the (111) direction, for eventually ZnO will be laid down on top of the Au, for the quality of the ZnO is dependent on the alignment of the Au crystallites. In turn, a ZnO layer approximately 1.5 μm thick is laid down along the full length (3 cm) of the device, and then at each end of the system, interdigital transducers are deposited for use as input transducers. In the middle region a thin transparent Au (approximately 200 Å) contact is laid down for optical imaging purposes. For a convolver this contact can, of course, be thicker.

Initially on the RADC contract, considerable effort was devoted to determining the optimum temperatures for growth of the ZnO layer. It was found that on Au the optimum temperature is approximately 225°C, whereas on SiO_2 the optimum temperature is about 250°C. These temperatures are critical if well aligned ZnO crystallites are to be obtained so that good piezoelectric coupling can be obtained.

We carried out a theoretical analysis to determine the convolution efficiency of this type of convolver. Both the optical sensitivity and the convolution efficiency tend to be maximum at approximately the same point.

The theory for the efficiency of the monolithic convolver was derived, initially, at flat band conditions. This theory takes into consideration

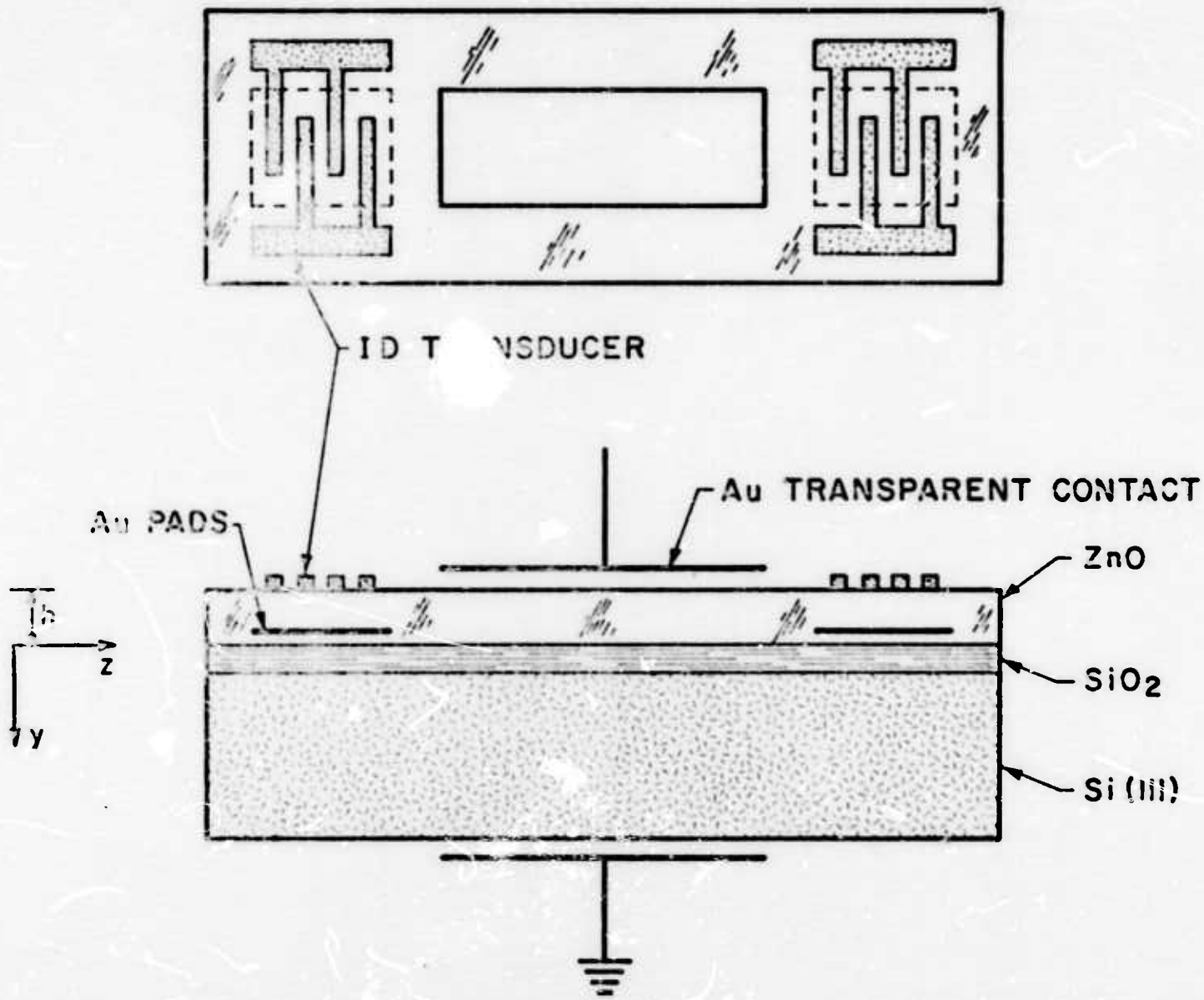

FIG. IV-1 -- Monolithic convolver with ZnO/Si.

the silicon dioxide layer between the zinc oxide film and the silicon substrate. The internal convolution efficiency is given by the relation

$$\mathcal{M} = [V_3/(P_1 P_2)^{1/2}]$$

$$\mathcal{M} = \frac{\sqrt{2}}{3} \frac{1}{qN_d} \frac{\omega}{v_a^2} \frac{\epsilon_0^2}{\epsilon_s} \frac{\left[1 + \frac{\beta \epsilon_0 \lambda_d}{\epsilon_0 M(\beta h)}\right]^{-2} \frac{\Delta v}{v}}{\left(\epsilon_{zz} + \sqrt{\epsilon_{xx}\epsilon_{zz}} \coth \sqrt{\frac{\epsilon_{xx}}{\epsilon_{zz}}} \beta h\right) M^2(\beta h, \beta d)} \qquad \text{(IV-1)}$$

where v is the voltage at the plate, and P_1, P_2 are the input powers per unit width. Similarly, the propagation loss per cm of silicon is given by the relation

$$\alpha_r = -\frac{1}{v} \frac{\dfrac{\omega_c \epsilon_s}{\epsilon_{zz} + \sqrt{\epsilon_{xx}\epsilon_{zz}} \coth \sqrt{\frac{\epsilon_{xx}}{\epsilon_{zz}}} \beta h} \frac{\Delta v}{v}}{1 + \left[\sqrt{\frac{\omega_c}{\omega}} + \frac{\omega_c}{\omega} \frac{\epsilon_s}{\epsilon_0} M(\beta h, \beta d)\right]^2} \qquad \text{(IV-2)}$$

where

$$M(\beta h, \beta d) = \frac{\epsilon_0}{\epsilon_s + \epsilon_{ox} \dfrac{\epsilon_{ox} \tanh \beta d + \sqrt{\epsilon_{xx}\epsilon_{zz}} \coth \sqrt{\frac{\epsilon_{xx}}{\epsilon_{zz}}} \beta h}{\epsilon_{ox} + \tanh \beta d \sqrt{\epsilon_{xx}\epsilon_{zz}} \coth \sqrt{\frac{\epsilon_{xx}}{\epsilon_{zz}}} \beta h}} \qquad \text{(IV-3)}$$

Here ϵ_0 is the free space dielectric constant, v_a is the surface acoustic wave velocity, and λ_d is the Debye length defined as $\lambda_d = (kT\epsilon_s/q^2 N_d)^{1/2}$,

ϵ_{xx} and ϵ_{zz} are the dielectric constants of ZnO in the x and z directions, respectively, $\Delta v/v$ is the coupling coefficient of ZnO on Si, h is the thickness of the zinc oxide film, d is the thickness of the silicon dioxide film, ϵ_{ox} is the dielectric constant of silicon dioxide, ω_c is the dielectric relaxation frequency defined as σ/ϵ_s, σ is the conductivity of the silicon, and ϵ_s is the dielectric constant of the silicon. This theory is valid for $f < 500$ MHz and $\sigma > 0.5$ ℧/m .

In Fig. IV-2, $\Delta\Omega$ and α_r are plotted as a function of the conductivity of the silicon for different values of d , the thickness of the silicon dioxide film. An optimum device is used so that, with loss taken into account, the efficiency is maximum.

Further developments of the theory indicate that the maximum convolution efficiency in this configuration occurs when the Si layer is depleted. This is in agreement with our experimental results and is a desirable characteristic for an optical imaging device in which carriers are generated in such a depletion layer, and the holes move through it to the surface to be stored at the surface in traps, thus giving a relative large storage time, and hence, high sensitivity.

It will be seen that in this configuration the convolution efficiency is maximum over a wide range of resistivities, but the optimum resistivity for a 1000 Å thick SiO_2 layer is approximately 30 ohm-cm. Consequently, we constructed our convolvers on 10 - 15 ohm-cm n-type material, the range of resistivities specified by the Si manufacturer, which is fairly near the optimum resistivity and is of a value in which it is possible to obtain high quality material. A few experiments have also been carried out on

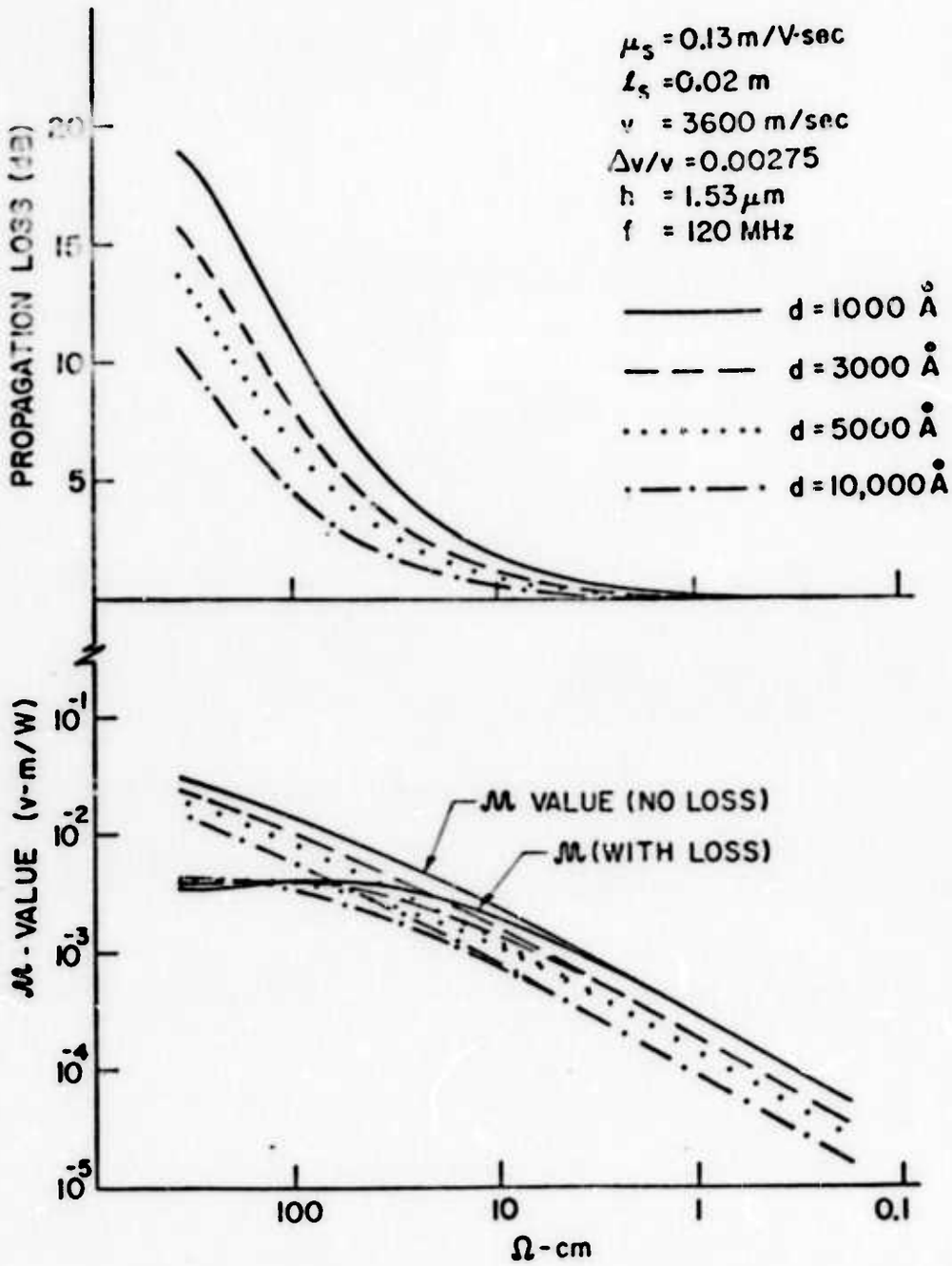

FIG. IV-2 -- Propagation loss per cm of silicon (α_r) and convolution efficiency (M), versus silicon conductivity (d = silicon dioxide film thickness). It will be seen that the M value with loss has a shallow maximum near [illegible] Ω-cm with d = 1000 Å.

epitaxial n on n^+ material, which we have grown in the Integrated Circuits Laboratory. This material has a 3 μm thick n layer and appears to be of higher quality for our purposes than the bulk material; it is more uniform, the resistance between the layer and the bottom contact is very small, and the layer itself appears to have fewer traps present. For the epitaxial layers, we measured the carrier density by Schottky barrier techniques, but the exact value of the resistivity of the samples used was not measured because convolution efficiency is almost constant over the range specified.

We used 10 finger pair transducers operated at an input frequency of 120 MHz. Because of the presence of the grounded silicon substrate, one side of the interdigital transducers must not be connected to ground, as this would mean that no field will exist between that side and the gold pad, and would not then contribute to the generation of the acoustic wave. We, therefore, feed the interdigital transducers through an unbalanced-to-balanced transformer (balun) and have designed and constructed a transformer of the type shown in Fig. IV-3. The output ends of the transmission line are both floating across two inductors to ground; these two inductors are equal if the transmission line and the wire have the same length. The output is then balanced. We have also designed and constructed a matching circuit to match the interdigital transducers to 50 Ω. The input circuitry is connected as shown in Fig. IV-4. With this configuration, the measured transducer-to-transducer loss was 18 dB. This is greater than its optimum value, because the capacitance between the transducer pads and the gold film underneath the ZnO tends to be too high.

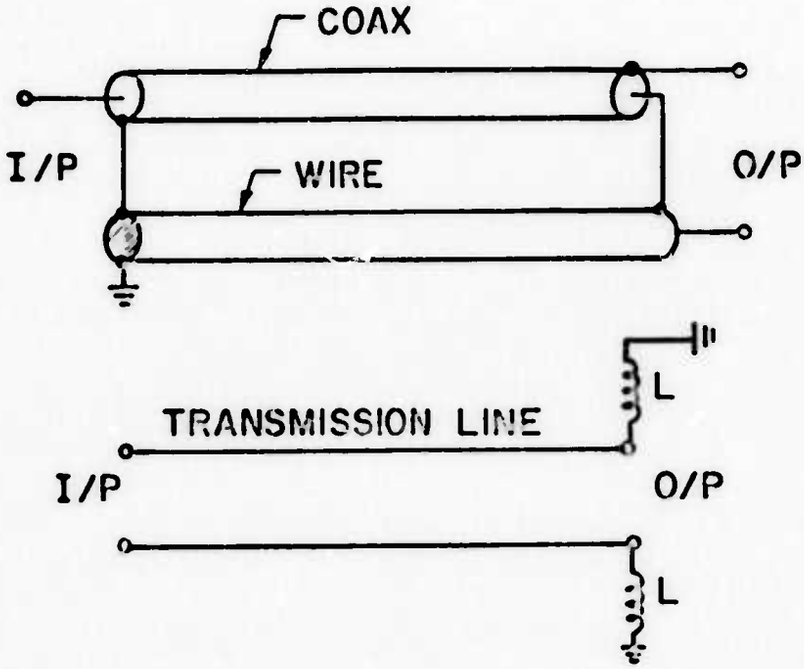

FIG. V-3 -- Schematic and equivalent circuit of balun.

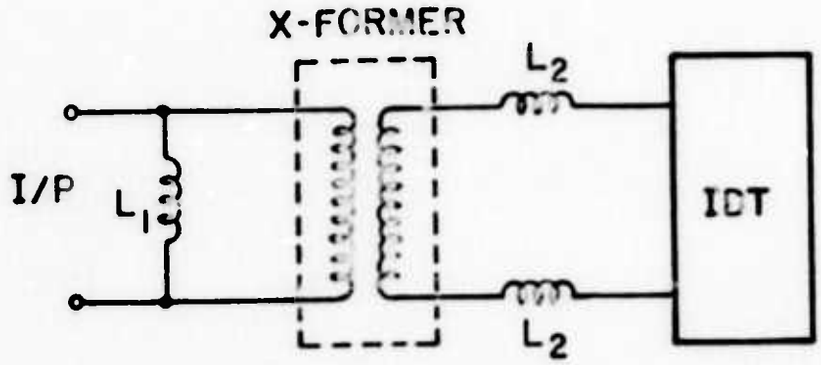

FIG. IV-4 -- Input matching circuit.

We now have the capability of making pads only a 2 mil × 2 mil and have made samples with a pad capacitance well below the interelectrode capacitance of the interdigital transducers themselves. This increases the effective radiation resistance from approximately 12 Ω to the theoretical value of 50 Ω. With such transducers operating in an unbalanced mode, we have obtained a terminal-to-terminal loss of 15 dB. We expect to reduce the terminal-to-terminal loss in the balanced mode to less than 12 dB.

With the use of the 18 dB transducer, a convolver with an efficiency of

$$F = P_{out}/P_{in_1} P_{in_2} = -58 \text{ dBm}$$

was constructed. This compares with the theoretically calculated value of -57 dBm, a very close fit. The present bandwidth of the device is 8 MHz. The results may also be compared with that of our best airgap convolvers for which F = -42 dBm . By reducing the loss of the transducers further, and by changing some of the parameters slightly, we expect to be able to obtain convolution efficiencies of better than -50 dBm, i.e., an output of -10 dBm with 20 dBm reference signals. This would give a 50 - 70 dB dynamic range in an optical imaging device.

We have observed a shift of the characteristics of the convolver due to the application of dc bias to the top place. This shift remains when bias is removed. We believe that this effect is due to driving ionic charges into the silicon dioxide, where they give rise to trap levels with a large time constant. We have grown a layer of silicon nitride between the zinc oxide and silicon dioxide in order to prevent this effect; it appears to perform the protective role expected. An additional effect

encountered at first was due to the long-time storage of charge generated when the applied fields were beyond the avalanche breakdown point. Now, with more careful attention to the applied fields and to the processing treatments employed, we appear to be able to eliminate the hysteresis with the use of silicon nitride.

We have carried out experiments to determine how these devices will perform as photosensors, but have not yet used them to obtain scanned images. So far, we have illuminated the total area of the semiconductor and determined how the efficiency is modulated. We have observed that we have been able to change the output efficiency of the convolver by 18 dB, i.e., we have obtained an 18 dB dynamic range. This compares very favorably with the airgap convolver in which the dynamic range is close to 10 dB when no grating is used in front of the convolver. In this configuration, we would of course expect to eventually place a grating on the top surface to obtain a large dynamic range, just as in the airgap convolver. This would be easy to do in this system, for the grating could be placed very close to the silicon surface in a further deposition.

The results obtained are only preliminary and are not optimized. The gold layer is probably thicker than it should be and, thus, the light passing through it is attenuated; we need to thicken up the edges of the gold layer so that its resistance will be lower along its length, thus making the device suitable for imaging in which a uniform high speed response is needed over the length of the film. A far more serious problem has been the fact that in the optical mode the results have not been highly reproducible, although the convolvers themselves are high reproducible. The basic problem here appears to be related to the presence of surface states

at the silicon dioxide-silicon interface. This leads to the presence of both slow and fast states. The slow states give rise to a long-term memory because charges are stored in them for periods which can extend up to days, thus accounting for the lack of reproducibility of the results. The fast states are useful in that they store charge and hence lead to more sensitivity, but it is difficult to control the uniformity of the surface states.

We do not believe that it is fruitful to try and meet the surface state problem head on. We are, therefore, adopting a different approach very similar to that adopted in the charge coupled device. Basically we are constructing our next devices using a large number of p-n junctions along the semiconductor surfaces; the nonlinear interaction now takes place in the buried junction rather than at the surface. This should avoid the whole problem associated with surface states and also give rise to extremely high sensitivity in the optical imaging device. Our work on this buried channel concept will be described in the next progress report.

At the same time, we are finishing up our improvements on the convolver configuration so as to operate with somewhat higher resistivities, of the order of 30 ohm-cm; this should give an efficiency of $F = -50$ dBm, or better. We are also designing new transducers to increase the bandwidth to 10 - 20 MHz. We propose to do this by decreasing the number of finger pairs and increasing the operating frequency.

V. FM CHIRP GENERATOR

Because of the specialized requirements placed on the sweepers in this experiment, it was felt that a specialized sweeper would be more appropriate than a general laboratory instrument. Thus, a design project was undertaken to meet these requirements. The sweeper must be capable of very high sweep rates (200 kHz/μsec), while maintaining extreme linearity (± 40 kHz from straight line). It was felt that the design would be simplified with the use of integrated circuit oscillator components by implementing the basic voltage controlled oscillator at 50 MHz, and then doubling to 100 MHz. The requirement for the 50 MHz VCO were sweep rates of up to 100 kHz/μsec and linearity of ± 20 kHz from straight line.

The basic circuit chosen for the VCO utilized a Motorola MC 1648 integrated circuit oscillator with a pair of hyper-abrupt junction varactor tuning diodes in the tank circuit. It was found experimentally that there was a narrow region over which the capacitance varied as $1/V^2$ (where V is the applied voltage) in a fashion which was sufficiently linear to allow the design requirements to be met. The problem here is that, while the diodes show approximately a $1/V^2$ characteristic, there is some error, and the deviations from the correct characteristic can be large.

Once the desired operating point on the diode was located, an inductor was chosen to give the desired center frequency. A control voltage buffer circuit was then constructed to allow the diodes to be biased at the proper point, and yet allow a sweep input voltage which varied about zero, so as to be able to keep the center frequency invariant while varying the sweep rate.

During the testing of the oscillator, it was found that there was a large temperature dependent frequency variation. It was determined that this variation came from three sources: the temperature coefficients of the tuning diodes, the input capacitance of the MC 1648, and the reference voltage for the diodes. The tuning diodes were placed in component ovens and the MC 1648 was put on a component heater to temperature stabilize them. The reference voltage was temperature stabilized by the use of a temperature compensated reference diode (1N4566).

With these additions, the VCO was then used with an internal bridge diode modulator followed by a power amplifier-doubler circuit to achieve the desired center frequency and bandwidth. The circuit is shown in Figs. V-1 and V-2.

These sweepers were found to perform as expected and will sweep well in excess of the desired rate, while still maintaining the required linearity over a slightly reduced bandwidth, as can be seen from the frequency deviation curves given in Fig. V-3.

FAST SWEEPER

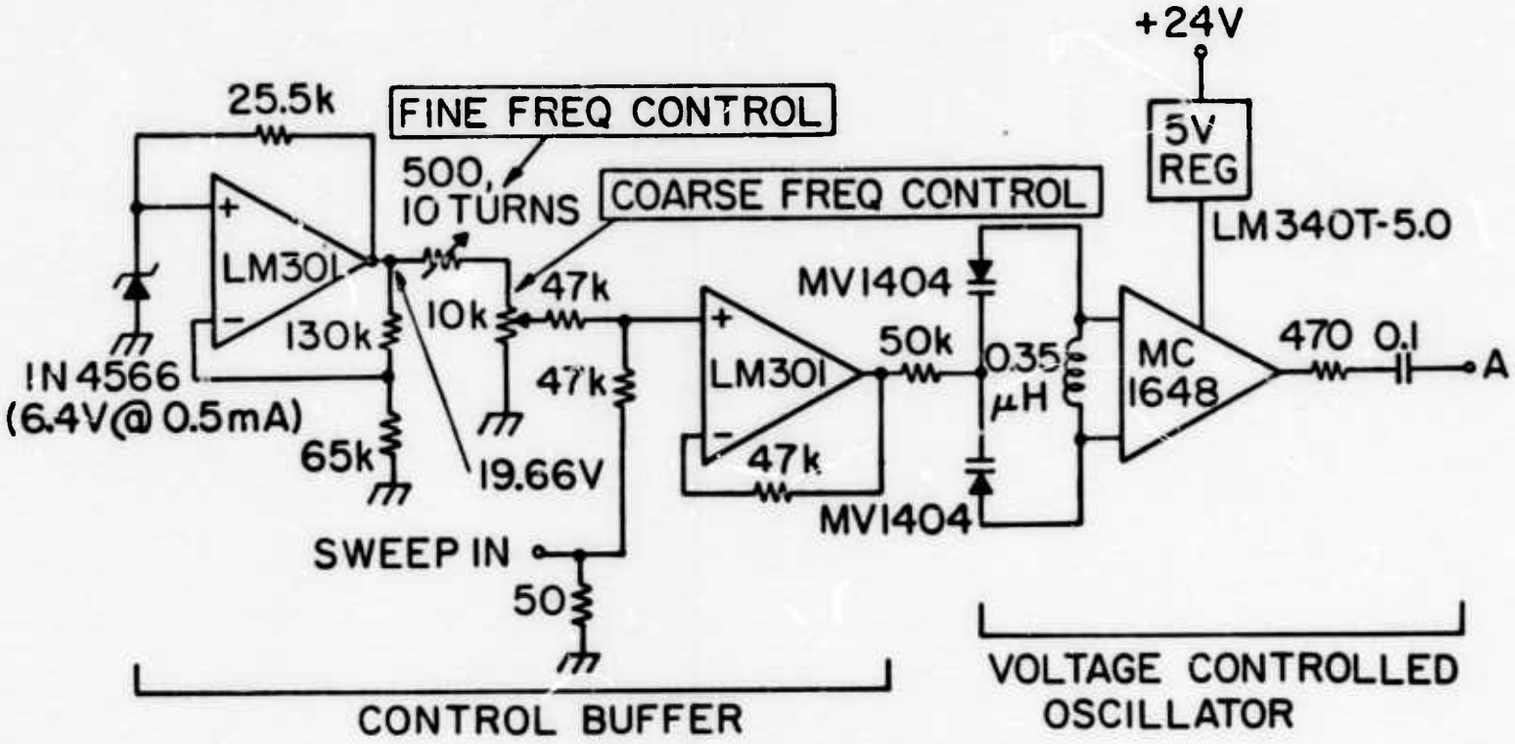

NOTE:

1. MV1404 DIODES MOUNTED IN OVENS (JERMYN-3STI-2)
2. MC1648 MOUNTED ON HEATER (JERMYN-7STI-1)
3. ALL FIXED RESISTORS ARE 1% METAL FILM

FIG. V-1 -- Fast sweeper circuit diagram.

FAST SWEEPER AMPLIFIER-DOUBLER

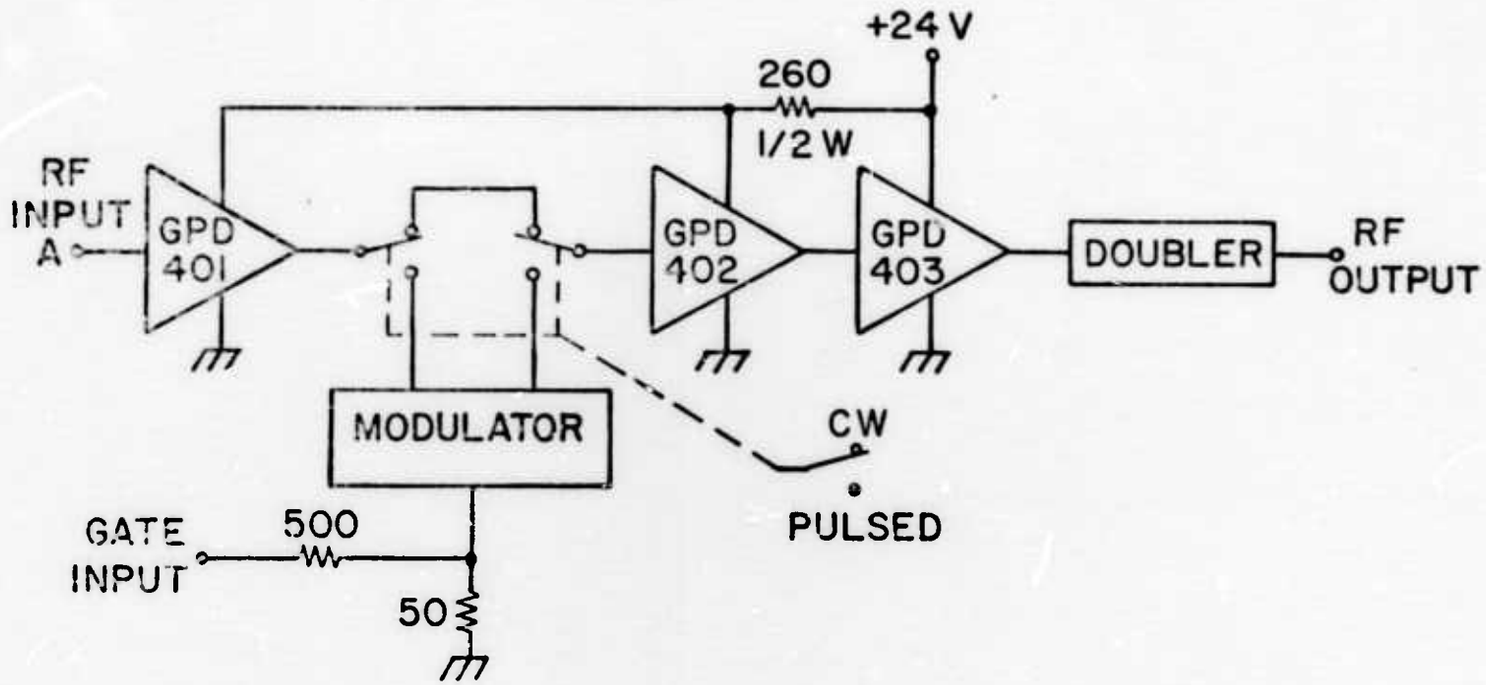

NOTE :

1. DOUBLER AND MODULATOR ARE MINI CIRCUITS SRA-1 DOUBLE BALANCED MIXERS

FIG. V-2 -- Fast sweeper amplifier doubler.

7212-3.

3212-5

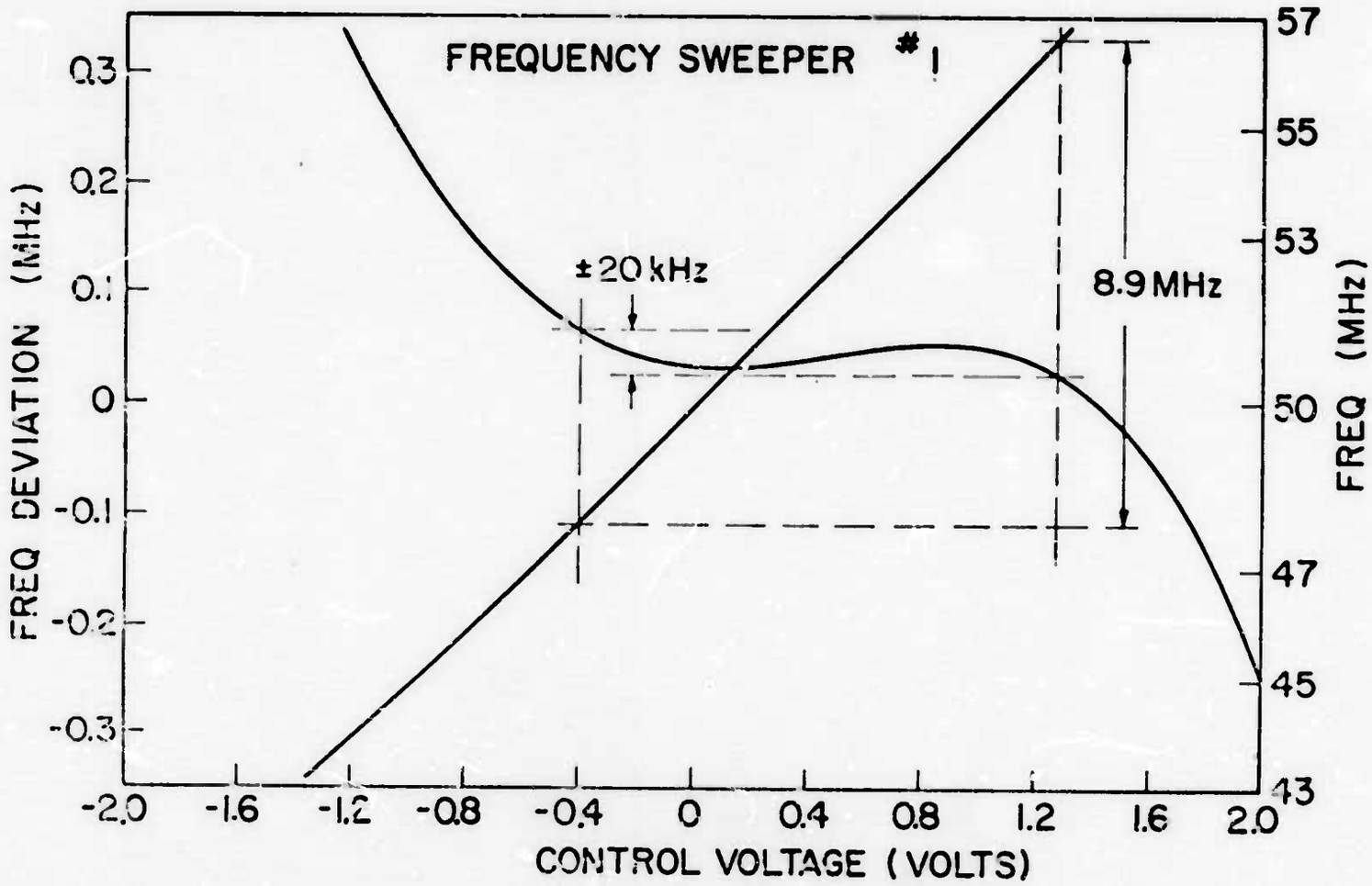

FIG. V-5 -- Experimental frequency deviation over the desired operating range.

APPENDIX

IMAGING BY TRANSFORM CODING

We give here a derivation of the mathematical results associated with the convolution and filtering processes that take place in the complete imaging system represented in Fig. II-8.

Notation:

L = length of the semiconductor

v = acoustic wave velocity

$T_A = L/v$ acoustic delay under the semiconductor.

The input chirped signals have the following characteristics:

- duration T_C
- chirp rate μ_1 and $-\mu_2$ in rd/s^2
- total input bandwidth $B_C = (\mu_1 + \mu_2)\, T_C/2\pi$
- dispersive filter bandwidth $B_s = (\mu_1 - \mu_2)\, T_C/2\pi$.

Convolver Output:

We take the center of the semiconductor as the origin $z = 0$. If the two input electrical signals are $f_1(t)$ and $f_2(t)$, the output voltage of the convolver $h(t)$ is given by

$$h(t) = \int_{-L/2}^{L/2} f_1(t - z/v)\, f_2(t + z/v)\, dz \quad . \qquad \text{(A-1)}$$

Now let f_1 and f_2 be the chirped signals of center frequency ω_1 and ω_2 and chirp rate μ_1 and $-\mu_2$, respectively:

$$f_1(t) = \exp j\left(\omega_1 + \frac{\mu_1 t}{2}\right)t \quad , \qquad \text{(A-2)}$$

and

$$f_2(t) = \exp j\left(\omega_2 - \frac{\mu_2 t}{2}\right)t \qquad \text{(A-3)}$$

Due to the presence of the grating, we assume no dark current and hence the output of the convolver is proportional to the light generated carrier density $n(z)$. We express this output as

$$h(t) = \exp(j\omega_3 t) \int_{-L/2}^{L/2} n(z) \exp j\left[\frac{\mu_1 - \mu_2}{2}\left(t^2 + \frac{z^2}{v^2}\right) - \frac{\mu_1 + \mu_2}{v} zt\right] dz \qquad \text{(A-4)}$$

The output corresponding to one spot of light at z_0 is obtained by letting $n(z) = \delta(z - z_0)$ in Eq. (A-4)

$$h_0(t) = \exp j\left[\omega_3 - \frac{\mu_1 + \mu_2}{v} z_0 + \frac{\mu_1 - \mu_2}{2} t\right]t \times \exp j\left(\frac{\mu_1 - \mu_2}{2}\right)\frac{z_0^2}{v^2}$$

$h_0(t)$ is chirped with a chirp rate $\mu_1 - \mu_2$ and its center frequency is a linear function of position

$$\omega(z) = \omega_3 - \frac{\mu_1 + \mu_2}{v} z \quad . \qquad \text{(A-5)}$$

$h(t)$ is also called the Fresnel Transform of $n(z)$. To reconstitute the original image $n(z)$, we must thus feed $h(t)$ into a filter matched to a chirp rate $\mu_1 - \mu_2$ and length T_C . The transfer function of such a filter can be written as follows:

$$F(\omega) = \exp\left(-j\frac{\omega|\omega|}{2(\mu_1 - \mu_2)}\right) \cdot \Pi\left[\frac{\omega - \omega_3}{(\mu_1 - \mu_2)T_C}\right] \qquad \text{(A-6)}$$

where Π is unity in the interval $[\omega_3 - (\mu_1 - \mu_2)T_C/2, \omega_3 + (\mu_1 - \mu_2)T_C/2]$ and zero outside it. We did not account for the linear phase factor in $F(\omega)$ which corresponds to a constant time delay; and we had to introduce an "absolute value" sign to ensure the hermiticity of the transfer function. In what follows, we shall only integrate over positive frequencies (thus introducing an extra factor 2) and we shall drop the absolute value sign.

Let $H(\omega)$ be the spectrum of $h(t)$, the output of the filter is

$$g(t) = \frac{1}{\sqrt{2\pi}} \int_{-\infty}^{+\infty} F(\omega)\, H(\omega)\, \exp(j\omega t)\, d\omega \tag{A-7}$$

with

$$H(\omega) = \frac{1}{\sqrt{2\pi}} \int_{-\infty}^{+\infty} h(t')\, \exp(-j\omega t')\, dt' \quad . \tag{A-8}$$

From Eqs. (A-4) through (A-8), $g(t)$ can be put in the form

$$g(t) = \frac{1}{2\pi} \int_{-L/2}^{+L/2} dz\, n(z)\, \exp\left[j\, \frac{\mu_1 - \mu_2}{2} \left(\frac{z}{v}\right)^2 \right]$$

$$\iint \exp j \left[\omega(z)t' - \omega(t' - t) + \frac{\mu_1 - \mu_2}{2}\, t'^2 - \frac{\omega^2}{2(\mu_1 - \mu_2)} \right] dt'\, d\omega \quad . \tag{A-9}$$

To compute the double integral over t', ω, we define the variables Ω, T

$$\Omega = \omega - \omega(z)$$

$$T = t' + \frac{j\Omega}{\mu_1 - \mu_2} \tag{A-10}$$

and rewrite $g(t)$ as:

$$g(t) = \frac{1}{2\pi} \int_{-L/2}^{L/2} dz\, n(z) \exp j \left[\frac{\mu_1 - \mu_2}{2} \left(\frac{z}{v} \right)^2 + \omega(z) t - \frac{\omega(z)^2}{2(\mu_1 - \mu_2)} \right]$$

$$\times \int_{-\infty}^{+\infty} \exp \left(j \frac{\mu_1 - \mu_2}{2} T^2 \right) dT$$

$$\times 2 \int_{\omega_3 - \omega(z) - \pi B_s}^{\omega_3 - \omega(z) + \pi B_s} \exp \left[j\Omega \left(t - \frac{\omega(z)}{\mu_1 - \mu_2} \right) \right] d\Omega \quad .$$

(A-11)

The integral over T is

$$\sqrt{\frac{2\pi}{\mu_1 - \mu_2}}\, e^{j\pi/4}$$

and the integral over Ω introduces a $\sin X/X$ function. After a few rearrangements we obtain

$$g(t) = \sqrt{B_s T_C} \exp \left[j\omega_3 (t - \tau_0) \right] \cdot \exp j \left(\frac{\pi}{4} + \frac{\tau_0}{2} \right)$$

$$\times \int_{-L/2}^{L/2} n(z) \cdot \frac{\sin \pi B_s (t - \tau_0 - z/v_s)}{\pi B_s (t - \tau_0 - z/v_s)} \exp \left[j \cdot \frac{\mu_1^2 + \mu_2^2}{\mu_1 - \mu_2} \cdot \left(\frac{z}{v} \right)^2 \right] dz \quad .$$

(A-12)

$\tau_0 = \omega_3/(\mu_1 - \mu_2)$ is the time delay in the dispersive filter at the center frequency ω_3 . The $\sin X/X$ function is the "scanning function". It is

peaked about the point $z = v_s(t - \tau_0)$, hence v_s is the actual scan velocity given by the relation

$$v_s = \frac{\mu_1 - \mu_2}{\mu_1 + \mu_2} v = v \frac{B_s}{B_C} \quad . \tag{A-13}$$

The 3 dB width of the "scanning function" defines the minimum resolvable spot d_s:

$$d_s = \frac{v_s}{B_s} = \frac{v}{B_C} \quad . \tag{A-14}$$

The number of resolvable spots is therefore given by

$$N = \frac{L}{d_s} = B_C T_A = B_s T_C \quad . \tag{A-15}$$

The last equality comes from the definitions of the velocities v and v_s ; we can indeed write

$$L = vT_A = v_s T_C \quad .$$

For medium-to-high resolution ($N \geq 30$), the scanning function is sharply peaked about $z = v_s(t - \tau_0)$. In this case it can be shown that over the center lobe of width $2d_s$, the phase error, in the integral of Eq. (A-12), is only π/N . We may therefore approximate the phase term in this integral by its value at $z = v_s(t - z_0)$. The limits of integration can also be removed to infinity if we consider that $n(z)$ is zero outside the interval $[-L/2, L/2]$. Finally, to obtain the amplitude of the reconstituted image, we approximate the scanning function by the dirac function

$$\frac{v_s}{B_s} \delta\left(z - v_s(t - \tau_0)\right) \quad .$$

Equation (A-16) follows:

$$g(t) = \sqrt{\frac{T_C}{B_s}}\, v_s\, n\big(v_s(t-\tau_0)\big) \exp - j\left[\frac{(\mu_1^2+\mu_2^2)(\mu_1-\mu_2)}{(\mu_1+\mu_2)^2}\cdot(t-\tau_0)^2 + \omega_3(t-\tau_0) + \frac{\pi}{4} + \frac{\tau_0}{2}\right] . \tag{A-16}$$

$g(t)$ is a replica of n, delayed by τ_0 and chirped with a chirp rate approximately equal to $\mu_1 - \mu_2$ and a center frequency ω_3.

<u>Comparison with the Direct Imaging System</u>

In a direct imaging system, a narrow pulse of width θ scans the semiconductor at a velocity v. The output is

$$g_{direct}(t) = \exp(j\omega_3 t) \int n(z)\, \Pi\left[\frac{t - z/v}{\theta}\right] dz .$$

The resolution is simply $v\theta$ and the number of resolvable spots $\frac{L}{v\theta} = \frac{T_A}{\theta}$. Besides the output bandwidth is θ^{-1}. The Π function can be approximated by $v\theta\, \delta(x - vt)$ and $g_{direct}(t)$ becomes

$$g_{direct}(t) = v\theta\, n(vt) \exp(j\omega_3 t) . \tag{A-17}$$

For a given resolution let us now compare the S/N ratio in the two systems.

In the chirp system the signal amplitude is given by Eq. (A-16) and the noise is proportional to the bandwidth B_s. In the direct imaging system the signal amplitude is given by Eq. (A-17) and the bandwidth used is θ^{-1};

hence

$$(S/N)_{\text{chirp system}} = \frac{v_s^2 \, T_C/B_s}{4kT \, B_s}$$

$$(S/N)_{\text{direct system}} = \frac{(v\theta)^2}{4kT\theta^{-1}} \quad .$$

Since the resolutions have to be identical, we can write $N = T_A\theta^{-1} = T_A B_C$. We then obtain the S/N improvement G provided by the Transform Coding of the image. G is given by

$$G = T_C B_C \quad . \tag{A-18}$$

We used Eq. (A-14). Equivalent forms for G are readily derived:

$$G = N\frac{T_C}{T_A} = N\frac{v}{v_s} = N\frac{B_C}{B_s} \quad . \tag{A-19}$$

<u>Design Curves</u>

We denote by a the dispersion of the reconstitution filter (in Hz/sec). By definition, $2\pi a = \mu_1 - \mu_2$. We call B_1 and B_2 the frequency excursion in the two input chirped signals so that $2\pi B_1 = \mu_1 T_C$ and $2\pi B_2 = \mu_2 T_C$. With these additional definitions we give below a summary of the results needed in designing the system:

$$a\,T_C = B_1 - B_2$$

$$B_C = B_1 + B_2$$

$$B_s = B_1 - B_2$$

$$N = B_s T_C = B_C T_A \quad .$$

We can express B_C, T_C and B_s in terms of the acoustic delay time T_A .

the filter dispersion a and the number of resolvable spots N. We obtain

$$B_C = N/T_A$$

$$T_C = (N/a)^{1/2}$$

$$B_s = (aN)^{1/2} .$$

Figure A-1(a) gives plots of B_C, T_C and B_s vs N in the particular experimental case where $T_A = 4$ μsec and a is 3 MHz/40 μsec. These plots allow us to determine B_1, B_2 and T_C, the chirp characteristics, to achieve any resolution N below 120. Figure A-1(b) gives plots of T_C and B_s vs a for the three resolutions $N = 120$, 200 and 300. If the line time T_C and the resolution N are given, one can therefore find what dispersive filter to use.

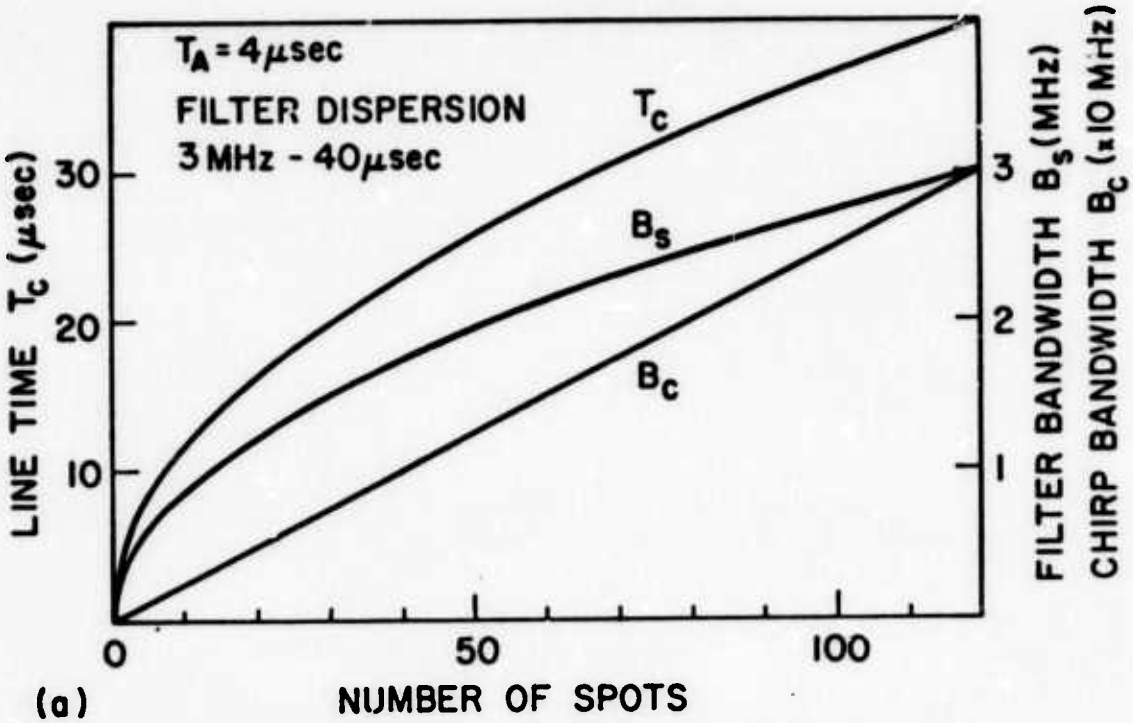

FIG. A-1--Design curves for the imaging system by Fresnel transforms.
(a) Line time, filter bandwidth and chirp bandwidth $T_A = 4$ μs and $a = 3$ MHz/40 μs.

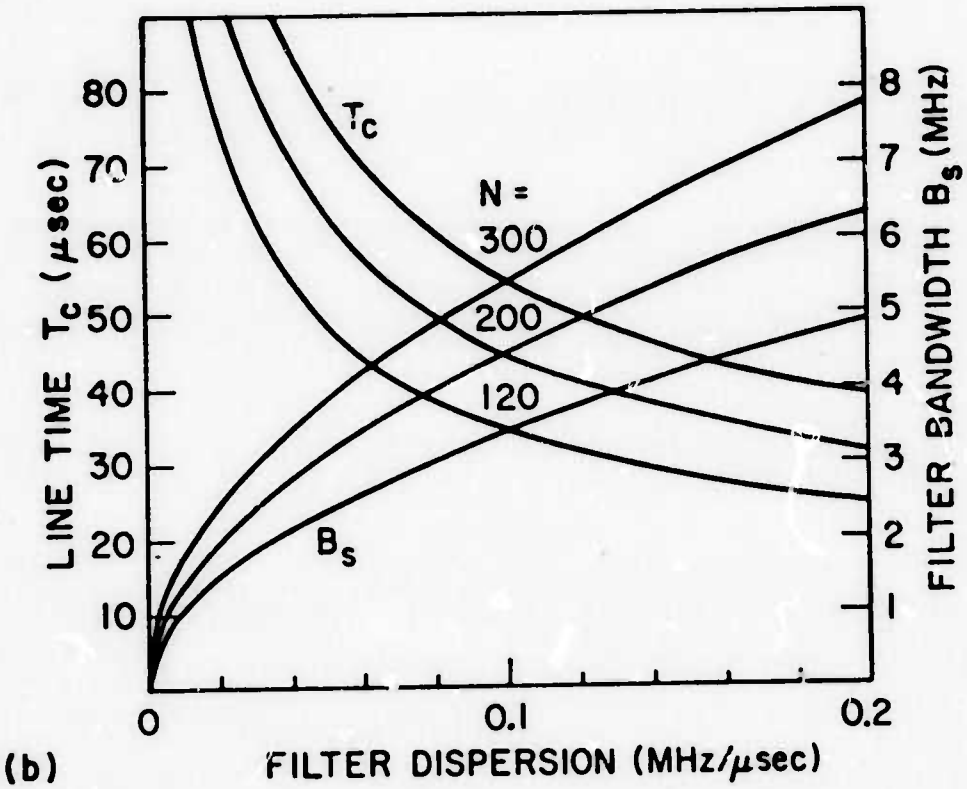

(b) Line time and filter bandwidth vs filter dispersion for various numbers of resolvable spots.

REFERENCES

1. G. S. Kino and H. Gautier, "Convolution and Parametric Interaction with Semiconductors," J. Appl. Phys. 44, 12, 5219-5221 (December 1973).
2. A. Many, Y. Goldstein, and W. B. Grover, "Semiconductor Surfaces," North-Holland Publishing Company (1965), Chapter II.
3. G. S. Kino and T. M. Reeder, "A Normal Mode Theory for the Rayleigh Wave Amplifier," IEEE Trans. Electron Devices, ED-18, 10, 909-920 (October 1971).
4. For example, P. L. Castro and B. E. Deal, "Low Temperature Reduction of Fast Surface State Charge (Q_{ss}) of Thermally Oxidized Silicon," J. Electrochemical Soc. 114, 225-274 (1967).